

Development of a Lensless Point-of-Care Device for Urine Analysis

DEVELOPMENT OF A LENSLESS POINT-OF-CARE DEVICE FOR URINE ANALYSIS

By

JESSICA KUN, B.Sc.

A Thesis

Submitted to the School of Graduate Studies

In Partial Fulfilment of the Requirements for the Degree

Master of Applied Science

McMaster University

©Copyright by Jessica Kun, April 2019

M.A.Sc Thesis – Jessica Kun

McMaster University – Biomedical Engineering

Master of Applied Science (2019)

McMaster University

School of Biomedical Engineering

Hamilton, Ontario

TITLE: Development of a Lensless Point-Of-Care Device for Urine Analysis

AUTHOR: Jessica Kun, B.Sc., McMaster University

SUPERVISOR: Professor Qiyin Fang

NUMBER OF PAGES:

Abstract

Clinical urine tests are valuable diagnostic tools for short and long-term patient care, however current detection techniques are time consuming and expensive. The turnaround time for samples tested for urinary tract infections is ~48 hours and 70% of samples are negative. Similarly, Trichomoniasis, a sexually transmitted infection caused by a vaginal pathogen, is misdiagnosed in clinical practice as symptoms are often similar to other conditions and conventional diagnostic tests are not readily available. Quick and accurate diagnosis of urologic and renal conditions is critical to their cost-effective management.

This dissertation focuses on the design, fabrication, and implementation of a lensless shadow imaging microscope for urine analysis. The device tested polystyrene beads, Baker's yeast, bacteria, whole blood, *Trichomoniasis vaginalis*, and urine samples. Unique and identifiable features were found for each component. To our knowledge, this is the first known report of lensless imaging for urine analysis. In particular, our device demonstrated effective detection of parasites directly in urine samples without the need for concentration or culture. With appropriate adaptations this platform can be developed to detect small particles in urine and contribute to patient diagnosis.

Acknowledgements

I would first like to thank my M.A.Sc supervisor, Dr. Qiyin Fang for everything he taught me, his thoughtful advice, all of the valuable learning opportunities he has provided throughout the last few years, as well as for his endless patience for my frequent requests for new image sensors. Thank you to Dr. Leyla Soleymani and Dr. Marek Smieja for the helpful discussions in each project meeting, and to Mark Gaskin who provided patient samples and answered any questions I had.

I would also like to thank everyone in the lab, Alex Ianovski, Colleen Chau, Eric Mahoney, Ian Phillips, Morgan Richards, Michael Zon, Fares Badr, Bo Xiong, for putting the FUN in bio-PHU(n)-tonics, and also for editing my thesis and discussing my hardware and image processing problems with me, that was greatly appreciated. Special thanks to Nehad Hirmiz and Dr. Samir Sahli for their insight in image processing. Many thanks to everyone for their helpful discussions in math, physics, and optical instrumentation.

Moreover, I would like to say thank you to Victor, Nadine, Rana, Celine, Rabia, and Maryam who have been always helpful and gave me such a great experience at McMaster throughout these years. Shout out to my roommates, mom and dad, who didn't know I was in an optics lab until last month.

Table of Contents

Abstract	iv
Acknowledgements	v
Table of Contents	vi
List of Figures	viii
List of Tables	xi
List of Abbreviations	xii
Chapter 1. Introduction	1
Chapter 2. Urinalysis	4
2.1. Urine Collection and Primary Analysis	4
2.2. Microscopic Urinalysis	5
2.3. Infections and Imbalances	7
2.3.1. Trichomoniasis.....	7
2.3.2. Bacterial Vaginosis	8
2.3.3. Vulvovaginal Candidiasis	9
2.3.4. Diagnostics in Hamilton General	9
2.4. Bacteriuria and Urinary Tract Infections	9
2.4.1. Culture.....	10
2.4.2. Fluorescence Flow Cytometry	11
2.4.3. Image-based Flow Cytometry.....	11
2.5. Discussion and Conclusion	12
References.....	13
Chapter 3. Lensless Imaging.....	16
3.1. Shadow Imaging	17
3.2. Fluorescence lensless imaging	19
3.3. Holographic lensless imaging.....	21
3.3.1. Back Propagation	22
3.3.2. Phase Retrieval	23
3.3.3. Digital In-line Holography as a Lensless Imaging Technique.....	23
3.4. Pixel Super Resolution.....	24
3.4.1. PSR in Optofluidics	26
3.5. Commercial Devices	26
3.6. Optical Devices for Urinalysis.....	26
3.7. Discussion and Conclusion	27
References.....	27
Chapter 4. Device Design, Fabrication, and Characterization.....	31
4.1. Development of a Urinalysis POC Device	31
4.1.1. Light Source.....	32
4.1.2. Detector.....	33
4.1.3. Plastic Thin Film for Static Images	35
4.1.4. Microfluidic Device for Optofluidic Imaging.....	35
4.1.5. PDMS Channel Fabrication and Optimization	36

4.1.6. Assembly.....	38
4.2. Device Characterization.....	39
4.2.1. 10µm Beads	40
4.2.2. 1µm Beads	41
4.2.3. Yeast	42
4.2.4. Blood Cells.....	43
4.2.5. E.coli	44
4.3. Discussion and Conclusion	44
References.....	46
Chapter 5. Urine Analysis	48
5.1. Trichomoniasis	48
5.1.1. Characteristics	48
5.1.2. Identification	50
5.2. Urinary Tract Infections.....	53
5.2.1. Identification	53
5.3. Crystals, Haline Casts, and Blood Cells	54
5.4. Discussion and Conclusion	55
References.....	57
Chapter 6. Summary and Discussion	58
6.1. Summary	58
5.2. Discussion.....	60
5.3. Future Directions	61
Appendix A: List of Supplementary Material.....	65

List of Figures

Figure 3.1: A Shadow Imaging Setup. A light source is placed several centimeters above the sample and detector. A transmissive sample is placed on the image sensor.	17
Figure. 3.2: Shadow images of <i>Euglena gracilis</i> (a–c), microspheres (d–f), and <i>Entamoeba invadens</i> cysts (g–o). The LR frames (top row) are directly from the device, with reconstructed HR frames below. Brightfield microscopy images taken with 20x objective lens are on the bottom row. Figure and caption derived from Zheng et al. [13].....	19
Figure 3.3: FlatScope setup. The FlatScope consists of an amplitude mask and 200 μ m spacer placed above an absorptive gel filter (not shown). The device is less than 1mm thick. A reconstruction algorithm is implemented to recover a high resolution image of the sample [22].	20
Figure 3.4: (a) Off-axis holography with a Mach-Zhender interferometer demonstrating the object and reference beam separation and recombination before their detection[25]. Samples within the object arm will produce interference upon recombination with the reference arm. (b) In-line holography demonstrating the interference effects from samples within the propagation space [26]. A light source (L) is shone through a pinhole (P). A spherical wave emerges(solid line) and passes around and through the objects (O) creating scattered waves (dashed lines). The scattered waves will interact with the reference waves and interfere creating interference patterns at the detector.	21
Figure 3.5 (a) Lensfree hologram of an immobilized semen sample (b) A bright-field microscope image of the same FOV as in (a) 40 \times objective-lens; NA: 0.65. (c,d) The reconstructed amplitude and phase images from (a). (e) Automatic detection of the sperm. Figure and caption derived from Su et al. [35]	24
Figure 3.6: (A) Confluent HeLa cell sample (B1 and C1) Raw images of a small region of A. (B2 and C2) The reconstructed high-resolution images corresponding to B1 and C1. (D) The conventional microscopy image, with 40 \times objective lens (0.66 N.A.). Figure and caption from Zheng et al. [11].....	25
Figure 4.1: (a) Optofluidic shadow imaging setup. Two adjustable C-clamps squeeze the microfluidic channel to the image sensor. (b)The sensor and channel are placed between a sensor holder and a transparent glass slide. This pressure is required to hold the channel flush and steady against the sensor, and the glass allows for the light to pass through to the channel. The distance between the light source and the detector is much larger (~30cm) than the distance between the sample and the detector (direct contact).	32
Figure 4.2: Simple LED lamp used as the incoherent broadband light source (Ikea, 003.859.41)	33
Figure 4.3: (a) Sony IMX219PQ image sensor with the plastic casing holding the lens and IR window removed. The casing is shown with the lens (top) and the IR filter (bottom, flipped) (b)	

Image sensor without lens and IR filter casing. (c) Gold bond wires are visible around the chip.35

Figure 4.4: The design and dimensions of the five channels. The lengths of the channels are all 5cm. Every channel was made with three different heights, 20 μ m, 50 μ m, and 80 μ m. A. Straight channel, 1mm in width. B. Two parallel channels 400 μ m wide with a 100 μ m divider between them for added support. C. 300 μ m wide “S” shaped channel. The full S spans the active area of the channel. D. Two parallel channels 475 μ m wide with a 50 μ m divider between them for added support. E. Straight channel, 500 μ m in width.36

Figure 4.5: Shadow imaging platform.39

Figure 4.6: Empty channel. The channel is not completely clear as PDMS itself contains particulates. It is also sticky and tends to attract dust and debris. There is a significant difference between the optical clarity when the PDMS thin film at the bottom of the channel is resting flush against the surface versus when it is not properly clamped, as can be seen on the left side of the image. Scale bar 250 μ m.40

Figure 4.7: (Left) 10 μ m polystyrene microbeads on a thin film of ~12 μ m. Scale 25 μ m (Right) The beads appear to have a size of around ~13.4 μ m.40

Figure 4.8: 10 μ m polystyrene beads in a water droplet on a plastic thin film. The size of the bead remains the same but the center of the bead is much brighter. Scale 25 μ m41

Figure 4.9: (Left) 10 μ m beads in a microfluidic channel with a height of 80 μ m. Scale 50 μ m (Right) The size of the beads now appears to be ~16.8 μ m.41

Figure 4.10: (Left) 1 μ m beads on a brightfield microscope with a 40 \times objective. Scale 10 μ m (Right) 1 μ m beads on the lensless platform. There are clear similarities between the images, however it is difficult to resolve the distances between the beads in the lensless image. Scale 10 μ m42

Figure 4.11: 1 μ m bead in a microfluidic channel on the lensless platform. Scale bar 5 μ m. .42

Figure 4.12: (a) (Top) Baker’s instant yeast *Saccharomyces cerevisiae* on a plastic thin film. Scale bar 30 μ m (Bottom) The diffraction of light through the yeast and onto the sensor is minimal as there is not a great enough distance between the yeast and the detector to allow the light rays to disperse (b) Baker’s instant yeast *Saccharomyces cerevisiae* in a microfluidic channel of height 80 μ m. Scale bar 30 μ m. (Bottom) The diffraction of light through the yeast and onto the sensor is larger as there is a larger distance between the yeast and the detector allowing the light rays to disperse43

Figure 4.13: (Top) Diluted blood flowing through the channel. The biconcave shape is an easy morphological feature to spot. The smaller, brighter particles in the image without the divot in the center are predicted to be damaged red blood cells. Scale bar 30 μ m. (Bottom) A red blood cell flipping as it moves along the channel. Scale 15 μ m44

Figure 4.14: E.coli in between a plastic thin film (b) E.coli in an 80 μm channel height. Overnight culture at 10^9 cfu/ml. Scale bar 30 μm 44

Figure 5.1: (a) Multiple *Trichomonas vaginalis* laid flat, parallel to the sensor. The characteristic morphology is visible in the image and its locomotion is visible in the video. Scale bar: 10 μm (b) Multiple *Trichomonas vaginalis* “standing” vertically in the channel, perpendicular to the sensor. Through visual analysis alone, there seems to be a change in intensity based on the orientation shift. The red bars in a and b indicate the axis through which the intensity histograms were created. Scale bar: 10 μm (c) A plot of the variation in intensity of the parasites in the horizontal and vertical orientations. There is a significant change in intensity between the two groups.49

Figure 5.2: (a) Trichomoniasis in a channel $>50\mu\text{m}$ from the sensor. The parasites lose the characteristic oblong morphology. Scale 50 μm . (b) Trichomoniasis in a channel $<20\mu\text{m}$ from the sensor. The parasites retain their oblong shape for the most part. Scale 50 μm50

Figure 5.3. Concise workflow of the algorithm for the processing of the lens-free shadow image. The algorithm consists of binarized image. Bottom pictures show how the original image is transformed at critical steps.51

Figure 5.4. One quarter of the full field of view of the microscope. Some parasites are not identified, as can be seen in the black boxes. These are false negatives in this frame, but are later identified in other frames. Scale 100 μm51

Figure 5.5. (a) Full field of view of *Trichomoniasis vaginalis* diluted in a urine sample and flown through the channel. (b) Full field of view of *Trichomoniasis vaginalis* being identified in the channel despite being diluted in a urine sample. Scale 200 μm 52

Figure 5.6. (a) Urine sample negating for bacteria. (b) Urine sample positive for bacteria ($>100\text{CFU}$). (c) Negative urine sample with background subtraction. (d) Positive urine sample with background subtraction. Scale 50 μm54

Figure 5.7: (a) Urine sample positive for the presence of bacteria. After background subtraction there is a significant amount of larger particles assumed to be damaged blood cells. (b) Urine sample negative for the presence of bacteria. After background subtraction there are few large particles. Scale 100 μm54

Figure 5.8: Calcium oxalate crystals found in urine under (a) a brightfield microscope [3] and (b) our lensless shadow imaging microscope55

Figure 5.9: Haline cast found in urine under (a) a brightfield microscope [3] and (b) our lensless shadow imaging microscope55

List of Tables

Table 2.1: A list of the different components of urine and their sizes, the subsequent diagnosis if found, and a microscopic image of the particle. Information was derived from *Simerville et al.* [2]. For more variations of different components, visit *Strasinger et al.* [3].....5

Table 2.2: A list of bacterial pathogens and their prevalence among inpatients and outpatients, modified from [32].....10

Table 4.1: Channel optimization. The 1000µm wide channel with a height of 80µm had the best flow and shape.38

List of Abbreviations

BV	Bacterial Vaginosis
CCD	Charge-coupled device
CFU	Colony forming units
CMOS	Complementary metal-oxide-semiconductor
FOV	Field of view
FPS	Frames per second
HPF	High powered field
HR	High resolution
LR	Low resolution
PCR	Polymerase chain reaction
PDMS	Polydimethylsiloxane
POC	Point of care
PSF	Point spread function
PSR	Pixel super resolution
RBC	Red blood cells
STI	Sexually transmitted infection
UTI	Urinary tract infection
WASP	Walk-away specimen processor
WBC	White blood cell

Chapter 1.

Introduction

Clinical urine tests are widely used diagnostic tools for a number of conditions including: urinary tract infections (UTIs) and trichomoniasis. UTIs, caused by the presence of bacteria in the urinary tract, are one of the most prevalent infections diagnosed through urinalysis. It affects almost 50% of the population at least once in their lifetime, leading to an annual health care cost of approximately \$3.5 billion in the USA [1]. In addition, there are a number of complicating factors associated with UTIs that can lead to urosepsis, a condition that has a mortality rate of 20%. Quick and accurate diagnosis is critical to the cost-effective management of UTIs, however, current detection techniques can take up to 48 hours and cost up to \$80 per test [2]. Trichomoniasis is a parasitic infection estimated to be the most common non-viral sexually transmitted infection (STI) in the world. It has recently been associated with poor reproductive outcomes and an increased risk of acquiring HIV. Trichomoniasis is often underdiagnosed and misdiagnosed in clinical practice as symptoms are often similar to other conditions and conventional diagnostic tests are not readily available [3].

Optical microscopes are a fundamental tool across science, engineering, and medicine. Microscopic imaging is a common diagnosis method for diagnosing UTIs and STIs from urine specimens, however, the microscopes are usually operated manually for image acquisition and analysis. Such low throughput approach subsequently requires amplification of the parasite/bacteria count through tissue culture of the urine specimens. The aim of this thesis is to discuss the development of a lensless optofluidic projection imaging device capable of automated urine analysis.

Lensless, or lens-free, microscopy records the image of the specimen on the detector without any intervening lenses. This allows for a large field of view, limited by the size of the detector, while maintaining sub-micron resolution, which is specific to the pixel size and post-imaging reconstruction. Lensless microscopes are also cost effective, and it allows for portability as there is no precise alignment needed. It is particularly well-suited to analysis applications in which a large quantity of specimens must be screened in order to determine whether a sample is positive or negative [4].

By integrating a microfluidic channel, a lensless optofluidic device is created and a large volume can be screened over a short period of time. One of the main advantages of using lensless imaging is the adaptability and cost effectiveness allowing these devices to be implemented as

point-of-care instruments for low-resource areas. It can also eliminate the need to culture every sample that comes through the regional microbiology laboratory by evaluating urine samples immediately after the sample was collected, resulting in a quicker turnover time, reduction in the administration of empirical antibiotics, and a lower operational cost [5]. If a sensitive and specific optical solution can be developed for urinalysis it could replace microscopy and simultaneously do trichomoniasis, candida and bacterial vaginosis testing in addition to UTI testing.

This dissertation presents lensless optofluidic microscopy as a rapid, low cost alternative to conventional techniques for processing urine. Current methodologies of urine analysis, the components of urine and their clinical significance, as well as current challenges associated with screening a large number of samples rapidly and accurately are outlined in chapter 2. Chapter 3 reviews different lensless imaging technologies and image processing algorithms presently found in the literature. By investigating the field of lensless imaging, we are able to better decide which method to use for our platform. Chapter 4 discusses the design, fabrication, and characterization of our developed lensless optofluidic system. Uniform samples of polystyrene microbeads, yeast, and blood were examined to determine how the platform views different specimen. Our results demonstrated that the prototype devices were able to test urine, which contains a mosaic of components, and cultured *Trichomoniasis vaginalis* parasites, which was described in chapter 5. Chapter six discusses the results from previous chapters and gives an overview of future outlook.

We developed a lensless shadow imaging prototype in combination with a microfluidic flow channel for the cost-effective rapid analysis of patient urine samples. We were able to demonstrate that our device can capture unique characteristics of yeast, red blood cells, bacteria, and *Trichomoniasis vaginalis* parasites for automated detection. To the best of our knowledge, this is the first time lensless microscopy has been used to do point-of-care diagnosis using unprocessed urine specimens. It was also the first attempt to identify free-floating bacteria with lensless imaging. In the future, we intend to complete the algorithms for automated detection of these components and enable the platform to diagnose patients with trichomoniasis and urinary tract infections.

References

- [1] M. Davenport, K. E. Mach, L. M. D. Shortliffe, N. Banaei, T.-H. Wang, and J. C. Liao, “New and developing diagnostic technologies for urinary tract infections,” *Nat. Rev. Urol.*, vol. 14, no. 5, pp. 296–310, May 2017.
- [2] F. M. Wagenlehner *et al.*, “Diagnosis and management for urosepsis,” *Int. J. Urol.*, vol. 20, no. 10, p. n/a-n/a, Jun. 2013.
- [3] G. E. Garber, “The laboratory diagnosis of *Trichomonas vaginalis*,” *Can. J. Infect. Dis. Med. Microbiol. = J. Can. des Mal. Infect. la Microbiol. medicale*, vol. 16, no. 1, pp. 35–8, Jan. 2005.
- [4] A. Ozcan and E. McLeod, “Lensless Imaging and Sensing,” *Annu. Rev. Biomed. Eng.*, vol.

18, no. 1, pp. 77–102, Jul. 2016.

- [5] K. Yasuma *et al.*, “Evaluation of a UF-1000i screening method to identify the bacteriuria for cultures and susceptibility testing,” *Rinsho Byori.*, vol. 60, no. 11, pp. 1070–4, Nov. 2012.

Chapter 2.

Urinalysis

Urinalysis is a valuable diagnostic tool for short and long-term patient care. It aids in the diagnosis of various urologic and renal conditions, and has the potential to provide evidence of complications in asymptomatic patients [1]. A complete urinalysis includes physical, chemical, and microscopic examinations of a urine sample. A physical examination includes visual analysis of the colour and odor of the urine, a chemical examination determines the pH and protein/chemical content of the sample, while microscopic examinations focus on the presence of large particles [2]. Various biomarkers are identified by these different levels of examination, and different tests have been implemented to detect these biomarkers to aid in patient diagnosis. A full comprehensive review of urinalysis can be found in Strasinger *et al.* [3]. This chapter will concentrate on detection at the microscopic level, specifically, the types of biomarkers that exist, the gold standard of tests that are used to detect them, and the future of urinalysis.

2.1 Urine Collection and Primary Analysis

Urine collection is routinely done in hospitals or clinics; however, they are typically not processed immediately. In some cases, there may be samples collected from a range of sites across a city that are then sent to one main clinical microbiological laboratory for testing[4]. In order to prevent spoiling or contamination of the sample, precautions are taken. The urine sample is collected mid-stream in order to reduce the amount of contamination from additional bacteria in the urinary tract and ensure collection of clean urine directly from the bladder. The urine must then either be refrigerated or examined within two hours as longer delay times often cause unreliable results [2].

A common, rapid, and cost-effective test that can be done on site is the dipstick test, which is often employed in cases where urinary tract infections (UTIs) are suspected. Dipsticks are instruments coated with reagents that change colour in the presence of an analyte, such as nitrite [2]. The benefit of such a test is that it only takes a few seconds to change colour, giving a preliminary diagnosis in real time. Extensive clinical studies and meta-analyses have been done to determine the diagnostic accuracy of the dipstick test. In general, they have shown that screening by dipstick alone carries the risk of missing infections and other urinary diseases. As such, they do not recommended dipsticks to be used as the sole diagnostic tool[5][6]. Urine dipsticks can give false-negative results in the case of dilute urine samples or samples in which

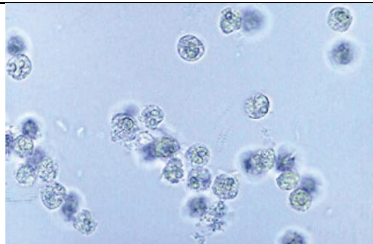
the pathogen does not produce nitrite, such as *Enterococcus* and *Staphylococcus* [6]. Thus, it is normally associated with other methods of urinalysis, and in many health care settings not performed as a point of care test, but in the clinical laboratory alongside further testing [7]. Urinary pH is also tested with a dipstick and is useful for the diagnosis of UTIs, as alkali urine indicates the potential presence of microorganisms breaking down urea. This, however, is not specific to UTIs and can indicate other ailments [2]. In order to get a more specific diagnosis, microscopic examination is employed.

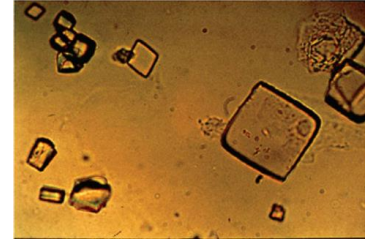
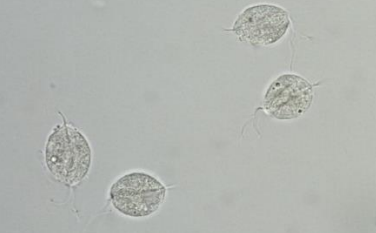
2.2 Microscopic Urinalysis

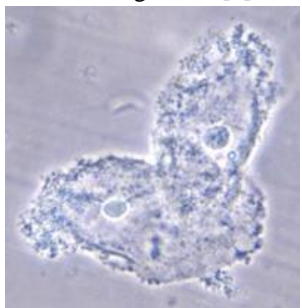
Through microscopic urinalysis, casts, cells, crystals, parasites, and bacteria can be identified and compounded with dipstick results for a more accurate diagnosis (Table 1). Brightfield microscopy is the most common method of microscopic urinalysis, though other techniques, like phase contrast, dark field and fluorescence are also employed. Normally, to prepare for microscopic urinalysis, a fresh 10-15mL sample of urine is centrifuged at 3000 rpm for five minutes to sediment particulate matter. Once finished, the supernatant is discarded and the sediment is resuspended and transferred to a glass slide and a coverslip is placed on top. Samples are then viewed under the microscope, and scored over 10 fields of view (FOV) at different magnifications [3].

With proper examination by a trained analyst, these elements can be distinguished from one another; however, without proper training, constituents may easily be misidentified. In addition, microscopic examination of urine samples is time consuming due to the number of FOVs that must be analyzed for each sample. Brightfield microscopy requires trained personnel and a minimum of 10 fields of view in multiple magnifications, making this a slow and tedious process [3]. Laboratories may need to analyze thousands of samples a week and the turnaround time per sample is 1-3 days.

Table 2.1: A list of the different components of urine and their sizes, the subsequent diagnosis if found, and a microscopic image of the particle. Information was derived from *Simerville et al.* [2] – Permission requested from the publisher. For more variations of different components, visit *Strasinger et al.* [3]

Component	Diagnosis	Size (um)	Image
Leukocytes (White Blood Cells)	- Normally, men have <2 WBC/HPF (high powered field) and women <5WBC/HPF	10-12	 <p>Normal WBCs [3]</p>

Erythrocytes (Red Blood Cells)	<ul style="list-style-type: none"> - >3 RBC/HPF in two of three urine samples suggests hematuria - If RBCs are dysmorphic, patient may have glomerular disease. 	6-8	
Epithelial cells	<ul style="list-style-type: none"> - Squamous epithelial cells suggests contamination - Transitional epithelial cells is normal - Renal tubule cells indicates significant renal pathology 	15+	
Casts	<ul style="list-style-type: none"> - Casts are used to localize disease to a specific location in the genitourinary tract depending on their composition - Hyaline casts can be associated with pyelonephritis or chronic renal disease. A full list of casts and associated conditions can be found in Simerville <i>et al.</i> [2]. 	15+	
Crystals	<ul style="list-style-type: none"> - Calcium oxalate crystals are normal - Uric acid crystals are normal - Triple phosphate crystals are associated with UTIs caused by Proteus - Cystine crystals are associated with cystinuria 	15+	
Bacteriuria	<ul style="list-style-type: none"> - In asymptomatic females 5 bacteria/HPF (roughly 100,000 colony forming units (CFU) per mL) represents asymptomatic bacteriuria - In symptomatic patients, 100 CFU per mL suggests UTI - In males, presence of bacteria is abnormal and culture should be obtained 	1-2	
Parasites	<ul style="list-style-type: none"> - Although less common, parasitic infections can also be detected in the urine. The two most common parasites that give rise to urological disorders are schistosomiasis (1 mm length) and <i>Trichomonas vaginalis</i> (10µm length). <i>Trichomonas vaginalis</i> often give rise to renal and lower urinary tract diseases, 	10µm-1mm	

Yeast	<p>and Schistosomiasis leads to permanent urogenital problems and renal failure [8].</p> <p>- The presence of budding yeast, <i>Candida albicans</i>, can be an indication of a yeast infection. They can be single, budding, or branched based on the severity of the infection.</p>	5-10	
Clue cells	<p>- Bacteria coats epithelial cells in an infection known as bacterial vaginosis. These cells are known as clue cells under the microscope and are a good indication of infection. Severity varies based on the extent of bacterial coverage.</p>	15+	

Budding Yeast [3]

Clue Cells; By CDC/ M. Rein [10],
via Wikimedia Commons

2.3 Infections and Imbalances

The presence or abnormal levels of non-metabolic components in urine may be indicative of an infection, microbial imbalance, or an underlying disorder. Changes in vaginal microbiota caused by the fungus *Candida* in yeast infections, or pathogenic bacterial populations like *E.coli* in bacterial vaginosis, are two common causes of infection. The presence of parasites like *Trichomoniasis vaginalis* is a common sexually transmitted infection (STI). Additionally, the presence of large amounts of bacteria in the urinary tract are indicative of urinary tract infections (UTI). These infections and imbalances have very similar clinical presentations and determining the pathogen responsible is critical to an accurate diagnosis.

2.3.1 *Trichomoniasis*

Trichomoniasis is estimated to be the most common non-viral STI in the world. Although it is not a reportable disease, and thus is not reported when diagnosed by doctors or laboratories, the World Health Organization estimated that in 2008 there were 276.4 million cases worldwide, making it more prevalent than *Chlamydia trachomatis*, *Neisseria gonorrhoeae*, and syphilis combined [11]. Although 85% [12] of women and 77% [13] of men are asymptomatic, *trichomoniasis* is associated with a number of other STIs [14], as well as poor birth outcomes [15] including low birth weight, preterm delivery, and intellectual disability in children [16][11]. Studies have indicated a higher risk for HIV acquisition among infected women [17][18]. In a

community with a high prevalence of trichomoniasis, as much as 20% of HIV cases could be attributed to the infection [19]. Controlling the incidence of trichomoniasis may be a cost-effective strategy for reducing the prevalence of HIV. If improperly diagnosed, trichomoniasis may persist for a number of years, with symptoms arising and subsiding over the course of the infection.

Trichomoniasis is an infection caused by *Trichomonas vaginalis*, a parasite 10–20µm in length and 2–14µm in width. It is often difficult to diagnose as symptoms are similar to other conditions and conventional diagnostic tests are not readily available [17]. It has commonly been diagnosed through wet mount microscopy, however the test must be read within 10 minutes of collection and sensitivities range from 50-70% depending on the technician performing the assay [20]. Culture has a higher sensitivity than wet mount, but it has been shown to be more expensive and time consuming. In two studies, it was found that after treating women positive for trichomoniasis, infection was undetectable for months via culture and then reappeared despite the absence of reported sexual exposure demonstrating the need for more sensitive testing [21][11]. The most sensitive tests are nucleic acid probe techniques, however, these are very expensive, require specialized instrumentation, and are not considered point-of-care.

There currently exist two point of care tests approved by the U.S. FDA for the diagnosis of Trichomoniasis among women: OSOM Trichomonas Rapid Test, which returns results in 10 minutes, and Affirm VP III, which takes 45 minutes. Both tests are performed after vaginal swabbing and have >83% sensitivity and >97% specificity [11]. The validation of OSOM Trichomonas Rapid Test is difficult and the Affirm VP III test is time consuming and requires instrumentation. Both are still too expensive for use by most medical centers.

2.3.2 Bacterial Vaginosis

Bacterial vaginosis (BV) is a common dysbiosis (microbial imbalance) which affects approximately 21 million women in the United States [22][23]. There has been research suggesting BV is associated with preterm labor and pelvic inflammatory disease [24] as well as contributes to the acquisition of STIs, including HIV [25][26]. Bacterial vaginosis is an overgrowth of atypical bacteria in the vagina. The environment of the vagina normally contains a high percent of lactobacilli and a small number of anaerobes, such as *G. vaginalis*, *Bacteroides*, or *Mobiluncus*. When an imbalance leads to too many anaerobes, it can result in bacterial vaginosis [23].

Vaginal swabs are used in the diagnosis of BV. Normally, a pH test and wet mount microscopy are done in order to measure an environmental pH greater than 4.5 and identify clue cells. Clue cells are vaginal squamous epithelial cells which are coated with the anaerobic bacteria causing BV [23]. Wet mount microscopy also has the added benefit of identifying trichomonas, yeast budding and clue cells for a differential diagnosis. Gram staining and Nugent scoring, which identifies and quantifies the bacterial species in a sample, is the gold standard for diagnosing BV; however, this method requires a laboratory in order to identify different bacteria [27]. Alternate tests can be used to diagnose bacterial vaginosis if microscopy is unavailable; however,

existing point-of-care tests are lengthy, expensive, and only indicate the presence of BV. An ideal test would be able to differentially identify BV, trichomoniasis, and yeast infections [23].

2.3.3 Vulvovaginal Candidiasis

Vulvovaginal candidiasis, commonly known as a yeast infection or candida, occurs when there is an imbalance and overgrowth of yeast in the vagina. This yeast, commonly known as *Candida*, is part of a normal microenvironment in many women and is often asymptomatic. Therefore, a yeast infection diagnosis is given when there is the presence of candida in the vagina as well as symptoms of irritation, itching, dysuria, or inflammation [28].

Around 70% of women report having vulvovaginal candidiasis at some point in their lifetimes, with *Candida albicans* being responsible for about 90% of cases [29]. Wet mount microscopy is the gold standard for the diagnosis of *Candida*, and if evidence of growth, such as budding yeast, or hyphae is seen, a yeast infection is confirmed [30].

2.3.4 Diagnostics in Hamilton General

The symptoms of these three ailments are similar, and their frequency in populations is quite high, thus, it is important to properly diagnose patients in order to treat them. Preferably, one test would be able to evaluate all three conditions. Hamilton General has previously evaluated OSOM Trichomonas Rapid Test for the diagnosis of trichomonas. The cost of the each test is around \$8-10 CAD. In an ideal scenario, \$2 CAD would be spent per test at Hamilton General to read trichomoniasis, candida, and bacterial vaginosis. The test has >83% sensitivity and >97% specificity and nucleic acid amplification tests, like polymerase chain reaction (PCR), is the gold standard; however, Hamilton General lacks a PCR machine to validate the test, as such equipment is quite expensive.

Most centers in Canada continue to do microscopy, and although it is a poor test when there has been a delay in getting specimens to the lab, it is still the best test for bacterial vaginosis and candidiasis, even if suboptimal for Trichomonas. Additional testing, whether antigen, culture, or molecular are done by some labs, but add cost and complexity. The BD Max multiplex PCR can test for all three conditions but costs around \$30 or more. If a sensitive and specific optical solution can be developed, it could replace microscopy and identify trichomoniasis, candida and potentially even bacterial vaginosis.

2.4 Bacteriuria and Urinary Tract Infections

Bacteriuria is defined as the presence of bacteria in the urine, however does not necessarily indicate an infection. Urinary tract infections (UTI), an infection caused by the presence of bacteria in the urinary tract, is extremely prevalent among communities and hospitals. They affect almost 50% of the population at least once in their lifetime, leading to an annual health care cost of approximately \$3.5 billion US dollars in the USA [7], 1.6 billion of which contributed to the administration of antibiotics [4], enhancing the risk of antibiotic resistance [31]. In addition, there are several complicating factors associated with UTIs that can affect

certain population groups like children, pregnant women, the elderly, and immunosuppressed patients. UTIs can be caused by a number of pathogens, though are most commonly caused by *Escherichia coli* and *Enterococcus* (Table 2). Fungal infections are not as common as bacterial infections, but are also possible. Quick and accurate diagnosis is critical to the cost-effective and personalized management of UTIs, however, current detection techniques are time consuming and expensive. *The presence of bacteria in the urine may also suggest a sexually transmitted infection (STI); the type of infection is dependent on the bacteria present.*

Table 2: A list of bacterial pathogens and their prevalence among inpatients and outpatients, modified from [32]

Pathogen Common in UTI's	Percentage of Outpatients with Pathogen	Percentage of Inpatients with Pathogen
<i>Escherichia coli</i>	53-72	17.5-56.7
<i>Coagulase-negative staphylococci</i>	2-7.5	2.1-12.5
<i>Klebsiella species</i>	6-12	6.2-15.0
<i>Proteus species</i>	4-6	3.8-8.2
<i>Enterobacter species</i>	0.6-5.8	0.9-6.5
<i>Morganella morganii</i>	3.1-4.4	4.7-6.0
<i>Citrobacter species</i>	0.1	0.2-3
<i>Enterococcus species</i>	1.7-12	6.5-15.8
<i>Staphylococcus aureus</i>	2	1.6-3.5
<i>Staphylococcus saprophyticus</i>	0.2-2	0.4
<i>Pseudomonas species</i>	0.1-4	1.3-11
<i>Candida species</i>	...	9.4-15.8
Other	3-8	1.8-26.3

2.4.1 Culture

The gold standard for the diagnosis of UTIs is urine culture, a method in which urine is placed on agar plates for growth and identification of present bacteria. Culture positives are generally those which grow $\geq 10^4$ cfu/ml of one species of bacteria [33]. Chromogenic agar allows for the identification of different bacteria including *Escherichia coli*, *Staphylococcus saprophyticus* and *Enterococcus* species by visually observing a colour change specific to each bacterial species after having been plated and grown [34]. Identification of other pathogens may require genotypic characterization of the bacteria. It takes between 18 and 30 hours to identify urine pathogens, with the initial overnight culture being the most time consuming step in the process [7].

Though effective, this solution is time consuming and of all samples being screened 60-80% are negative [35]. Automated culturing, such as the WASP (Walk-Away Specimen Processor, used in Hamilton General), has reduced the workload, but has not decreased the need for an alternative processing method. A solution to unnecessary culturing of samples is a screening test prior to culture with a high negative predictive value, ensuring that a sample determined to be negative is truly negative. In an effort to improve the efficacy of urinalysis, several alternative screening methods like fluorescence and image-based flow cytometry have been developed. These techniques are a preliminary screen that aim to reduce the number of samples cultured,

reducing the workload, time, and costs in large laboratories. In addition, negative results are informed earlier which reduces broad spectrum antibiotic prescriptions [36].

Hamilton General processes about 250 urine specimens a day and 60-70% show no growth. The average cost to analyze a positive urine sample is \$16.17, and for a negative urine sample it is about \$3 for the plate plus the minimal cost of the technician's time. The entire WASPlab system, with incubators and digital imaging included, is \$1.6 million.

2.4.2 Fluorescence Flow Cytometry

Fluorescence flow cytometry is a method by which cells are optically screened to rapidly determine chemical and physical properties of urinary constituents [37]. The urine sample is stained with fluorescent dyes, which bind to nucleic acids, and delivered to two different chambers: microorganisms and other. This prevents any interference in the analysis. There the hydrodynamically focused samples are illuminated with diode laser of appropriate wavelength and the intensity of emitted fluorescent signal and forward- and side-scattered light is examined. Forward scatter provides information on particle size, while side scatter dictates surface and internal complexity, and fluorescent signal informs on nucleic acid contents. RBCs, WBCs, squamous epithelial cells, casts, bacteria, yeast-like cells, spermatozoa, and crystals are identified and counted. Stained bacteria are determined as gram positive or negative. The software from the cytometer presents the data as identified particles per field of view or particles per microliter [37].

A thorough meta-analysis of the use of flow cytometers as a tool for urinalysis was conducted by Díaz-Gigante et al. in 2017, where studies using the UF1000i (Sysmex) analyzer as a pre-screening technique for urinalysis were analyzed [4]. They have shown a 28%-60% reduction in the number of processed samples when pre-screened with flow cytometry. Savings of \$239-\$306 USD per 100 samples have also been reported, indicating the use of a flow cytometer is cost efficient [38]. A significant reduction of turnaround time of negative cultures is noted, which leads to a decrease in empirical antibiotic prescription.

Although there are significant benefits to this pre-screening approach, there are certain caveats to this flow cytometry system. The performance of the screening process depends on the cut-off criteria applied to the patients, which is highly dependent on the population being analyzed. Published data recommended adjusting the cutoff values of the screens according to the clinical situation of the patients as well as the type of specimen collection in order to implement fluorescence flow cytometry as an effective screen [4].

2.4.3 Image-based Flow Cytometry

Image-based flow cytometry is another technique being used to reduce the number of cultured samples. The Iris iQ200 is an FDA approved automated urine microscopy analyzer that has been tested as an alternative to manual microscopy. In the Iris iQ200, urine samples are hydrodynamically focused between two layers of fluid in order to create a planar flow. Particles in the urine are analyzed as they pass under an objective lens that is used to focus on the particles

and capture 500 frames per sample [37], [39], [40]. The images are captured on a CCD camera and a neural network algorithm classifies particles based on shape, size, texture and contrast. The software displays the images for the operator to view and reclassify them if necessary. Particles are classified into the following categories: RBC, white blood cells (WBC), squamous epithelial cells, non-squamous epithelial cells, hyaline casts, non-hyaline casts, bacteria, crystals, yeast, sperm and mucus. Images that contain particles that are not identified to be a part of one of these categories are collected separately and are classified by a trained analyst. The lower limit for particle detection and quantification has been reported to be about 20 – 30 particles/ μl [37]. One caveat of the system is that at times, the images may appear out of focus to the analyst, and the image cannot be improved as the sample has already left the flow chamber.

A study analyzing the Iris iQ200 as a urinalysis screen found that the Iris iQ200 results were similar to the result of manual microscopic examination [41]. There were however, uncertain cases (particularly dysmorphic cells, bacteria, yeasts, casts and crystals), in which images had to be reexamined by trained staff. This indicates that trained staff is still necessary in the implementation of this screen, and the software requires further development to be fully automated. With these modifications, similar to the findings for the UF1000i, the authors concluded that automated systems would be helpful in terms of time saving and standardization.

2.5 Conclusion

Urine analysis is a critical diagnostic tool used in health care. Currently there are separate tests for different pathogens and they cost up to \$80 and take up to 48 hours. For urinary tract infections, far too many negative samples are being processed, which is an excessive waste of time and resources. Trichomoniasis is a very prominent STI that is often underdiagnosed due to the lack of a conventional test [17]. A device that can quickly eliminate negative samples from further processing would be able to significantly reduce costs, and administer earlier and more appropriate treatments to patients. A universal test for a variety of pathogens would reduce the rate of misdiagnosis.

Flow cytometry is being developed and tested as preliminary screens for urinalysis, and point-of-care tests have been developed for the diagnosis of trichomoniasis, bacterial vaginosis and *vulvovaginal candidiasis*. Though there has been progress in this area, rapid and cost-effective diagnosis is not yet routine. In this dissertation, we present the development of a point-of-care device that aims to reduce the turnaround time for samples, decrease the health care costs, and decrease the workload in labs. Turnaround time is crucial for the comfort and diagnosis of the patient as well as for the overloaded lab, and pre-screening techniques bypass the initial overnight urine culture thereby eliminating the most time consuming step. By filtering out negative samples early from the screening process, unnecessary culturing is avoided, as well as the potential pre-emptive deliverance of antibiotics. Ideally, this device would be implemented as a point-of-care device in hospital rooms and clinics to reduce the number of samples being sent to the lab, as well as allowing for personalized diagnosis as the clinical situation of the patient is immediately apparent. Our solution for this problem is the development of a lensless projection

imaging microscope, an easy-to-use, cost effective, point-of-care device, discussed in the following chapters.

References

- [1] G. B. Fogazzi, *The Urinary Sediment : An Integrated View*, 3ed ed., vol. 78, no. 12. Elsevier Srl, 2010.
- [2] J. A. Simerville, W. C. Maxted, and J. J. Pahira, “Urinalysis: a comprehensive review.,” *Am. Fam. Physician*, vol. 71, no. 6, pp. 1153–62, Mar. 2005.
- [3] S. K. Strasinger, M. S. Di Lorenzo, and M. Di Lorenzo, *Urinalysis and body fluids*. 2014.
- [4] P. Mejuto, M. Luengo, and J. Díaz-Gigante, “Automated Flow Cytometry: An Alternative to Urine Culture in a Routine Clinical Microbiology Laboratory?,” *Int. J. Microbiol.*, vol. 2017, pp. 1–8, Sep. 2017.
- [5] G. J. Williams, P. Macaskill, S. F. Chan, R. M. Turner, E. Hodson, and J. C. Craig, “Absolute and relative accuracy of rapid urine tests for urinary tract infection in children: a meta-analysis.,” *Lancet. Infect. Dis.*, vol. 10, no. 4, pp. 240–50, Apr. 2010.
- [6] W. L. Devillé, J. C. Yzermans, N. P. van Duijn, P. D. Bezemer, D. A. van der Windt, and L. M. Bouter, “The urine dipstick test useful to rule out infections. A meta-analysis of the accuracy,” *BMC Urol.*, vol. 4, no. 1, p. 4, Dec. 2004.
- [7] M. Davenport, K. E. Mach, L. M. D. Shortliffe, N. Banaei, T.-H. Wang, and J. C. Liao, “New and developing diagnostic technologies for urinary tract infections,” *Nat. Rev. Urol.*, vol. 14, no. 5, pp. 296–310, May 2017.
- [8] N. Mor, Ü. Y. Tekdoğan, and M. Bağcıoğlu, “Parasitic Diseases of Urinary Tract,” *MIDDLE BLACK SEA J. Heal. Sci.*, vol. 2, no. 3, pp. 11–18, 2016.
- [9] B. Šoba, M. Skvarč, and M. Matičič, “Trichomoniasis: a brief review of diagnostic methods and our experience with real-time PCR for detecting infection,” *Acta Dermatovenerologica Alp. Pannonica Adriat.*, vol. 24, no. 1, Mar. 2015.
- [10] Wikipedia, “Clue Cell,” 2018. [Online]. Available: https://en.wikipedia.org/wiki/Clue_cell.
- [11] P. Kissinger, “Trichomonas vaginalis: a review of epidemiologic, clinical and treatment issues,” *BMC Infect. Dis.*, vol. 15, no. 1, p. 307, Dec. 2015.
- [12] M. Sutton, M. Sternberg, E. H. Koumans, G. McQuillan, S. Berman, and L. Markowitz, “The Prevalence of Trichomonas vaginalis Infection among Reproductive-Age Women in the United States, 2001-2004,” *Clin. Infect. Dis.*, vol. 45, no. 10, pp. 1319–1326, Nov. 2007.
- [13] A. C. Sena *et al.*, “Trichomonas vaginalis Infection in Male Sexual Partners: Implications for Diagnosis, Treatment, and Prevention,” *Clin. Infect. Dis.*, vol. 44, no. 1, pp. 13–22, Jan. 2007.
- [14] J. E. Allsworth, J. A. Ratner, and J. F. Peipert, “Trichomoniasis and Other Sexually Transmitted Infections: Results From the 2001–2004 National Health and Nutrition

- Examination Surveys,” *Sex. Transm. Dis.*, vol. 36, no. 12, pp. 738–744, Dec. 2009.
- [15] B. J. Silver, R. J. Guy, J. M. Kaldor, M. S. Jamil, and A. R. Rumbold, “Trichomonas vaginalis as a Cause of Perinatal Morbidity,” *Sex. Transm. Dis.*, vol. 41, no. 6, pp. 369–376, Jun. 2014.
- [16] J. R. Mann, S. McDermott, T. L. Barnes, J. Hardin, H. Bao, and L. Zhou, “Trichomoniasis in Pregnancy and Mental Retardation in Children,” *Ann. Epidemiol.*, vol. 19, no. 12, pp. 891–899, Dec. 2009.
- [17] G. E. Garber, “The laboratory diagnosis of Trichomonas vaginalis.,” *Can. J. Infect. Dis. Med. Microbiol. = J. Can. des Mal. Infect. la Microbiol. medicale*, vol. 16, no. 1, pp. 35–8, Jan. 2005.
- [18] P. Kissinger and A. Adamski, “Trichomoniasis and HIV interactions: a review,” *Sex. Transm. Infect.*, vol. 89, no. 6, pp. 426–433, Sep. 2013.
- [19] F. Sorvillo and P. Kerndt, “Trichomonas vaginalis and amplification of HIV-1 transmission,” *Lancet*, vol. 351, no. 9097, pp. 213–214, Jan. 1998.
- [20] M. A. Kingston, D. Bansal, and E. M. Carlin, “‘Shelf life’ of <I>Trichomonas vaginalis</I>,” *Int. J. STD AIDS*, vol. 14, no. 1, pp. 28–29, Jan. 2003.
- [21] M. Gatski *et al.*, “Patient-delivered partner treatment and Trichomonas vaginalis repeat infection among human immunodeficiency virus-infected women.,” *Sex. Transm. Dis.*, vol. 37, no. 8, pp. 502–5, Aug. 2010.
- [22] E. H. Koumans *et al.*, “The prevalence of bacterial vaginosis in the United States, 2001–2004; associations with symptoms, sexual behaviors, and reproductive health.,” *Sex. Transm. Dis.*, vol. 34, no. 11, pp. 864–9, Nov. 2007.
- [23] P. Bagnall and D. Rizzolo, “Bacterial vaginosis: A practical review,” *J. Am. Acad. Physician Assist.*, vol. 30, no. 12, pp. 15–21, Dec. 2017.
- [24] B. D. Taylor, T. Darville, and C. L. Haggerty, “Does Bacterial Vaginosis Cause Pelvic Inflammatory Disease?,” *Sex. Transm. Dis.*, vol. 40, no. 2, pp. 117–122, Feb. 2013.
- [25] C. R. Cohen *et al.*, “Bacterial Vaginosis Associated with Increased Risk of Female-to-Male HIV-1 Transmission: A Prospective Cohort Analysis among African Couples,” *PLoS Med.*, vol. 9, no. 6, p. e1001251, Jun. 2012.
- [26] R. M. Brotman *et al.*, “Bacterial vaginosis assessed by gram stain and diminished colonization resistance to incident gonococcal, chlamydial, and trichomonal genital infection.,” *J. Infect. Dis.*, vol. 202, no. 12, pp. 1907–15, Dec. 2010.
- [27] K. Anukam, C. Idemoh, and N. Olise, “Evaluation of bacterial vaginosis (BV) using Nugent scoring system,” *J Med Biomed Res.*, vol. 13, no. 1, pp. 25–32, 2014.
- [28] B. Gonçalves, C. Ferreira, C. T. Alves, M. Henriques, J. Azeredo, and S. Silva, “Vulvovaginal candidiasis: Epidemiology, microbiology and risk factors,” *Crit. Rev. Microbiol.*, vol. 42, no. 6, pp. 905–927, Nov. 2016.
- [29] J. D. Sobel, “Recurrent vulvovaginal candidiasis,” *Am. J. Obstet. Gynecol.*, vol. 214, no.

- 1, pp. 15–21, Jan. 2016.
- [30] R. Jeanmonod and D. Jeanmonod, *Candidiasis, Vaginal (Vulvovaginal Candidiasis)*. StatPearls Publishing, 2018.
- [31] A. Sorlozano *et al.*, “Evolution of the resistance to antibiotics of bacteria involved in urinary tract infections: A 7-year surveillance study,” *Am. J. Infect. Control*, vol. 42, no. 10, pp. 1033–1038, Oct. 2014.
- [32] M. L. Wilson and L. Gaido, “Laboratory Diagnosis of Urinary Tract Infections in Adult Patients,” *Clin. Infect. Dis.*, vol. 38, no. 8, pp. 1150–1158, Apr. 2004.
- [33] C. M. Kunin and C. M. Kunin, *Urinary tract infections : detection, prevention, and management*. Williams & Wilkins, 1997.
- [34] H. A. D’Souza, M. Campbell, and E. J. Baron, “Practical bench comparison of BBL CHROMagar Orientation and standard two-plate media for urine cultures.,” *J. Clin. Microbiol.*, vol. 42, no. 1, pp. 60–4, Jan. 2004.
- [35] M. A. C. Broeren, S. Bahçeci, H. L. Vader, and N. L. A. Arents, “Screening for urinary tract infection with the Sysmex UF-1000i urine flow cytometer.,” *J. Clin. Microbiol.*, vol. 49, no. 3, pp. 1025–9, Mar. 2011.
- [36] W. J. McIsaac, D. E. Low, A. Biringer, N. Pimlott, M. Evans, and R. Glazier, “The impact of empirical management of acute cystitis on unnecessary antibiotic use.,” *Arch. Intern. Med.*, vol. 162, no. 5, pp. 600–5, Mar. 2002.
- [37] J. Delanghe, “New Screening Diagnostic Techniques In Urinalysis,” *Acta Clin. Belg.*, vol. 62, no. 3, pp. 155–161, Jun. 2007.
- [38] K. Yasuma *et al.*, “Evaluation of a UF-1000i screening method to identify the bacteriuria for cultures and susceptibility testing,” *Rinsho Byori.*, vol. 60, no. 11, pp. 1070–4, Nov. 2012.
- [39] S. Linko, T. T. Kouri, E. Toivonen, P. H. Ranta, E. Chapoulaud, and M. Lalla, “Analytical performance of the Iris iQ200 automated urine microscopy analyzer,” *Clin. Chim. Acta*, vol. 372, no. 1–2, pp. 54–64, Oct. 2006.
- [40] L. Alves, F. Ballester, J. Camps, and J. Joven, “Preliminary evaluation of the Iris IQ™ 200 automated urine analyser,” *Clin. Chem. Lab. Med.*, vol. 43, no. 9, pp. 967–70, Jan. 2005.
- [41] F. D. İnce, H. Y. Ellidağ, M. Koseoğlu, N. Şimşek, H. Yalçın, and M. O. Zengin, “The comparison of automated urine analyzers with manual microscopic examination for urinalysis automated urine analyzers and manual urinalysis,” *Pract. Lab. Med.*, vol. 5, pp. 14–20, Aug. 2016.

Chapter 3.

Lensless Imaging

In conventional microscopy, the use of lenses is critical to magnify the image of the specimen under observation. Microscopes are a standard instrument in labs across multiple disciplines, adaptable to the specific task they aim to complete. However, imaging without lenses is beginning to take shape as a competitive alternative, offering advantages like low-cost, large field of view, 3D reconstruction, and portability. Lensless, or lens-free, microscopy records the image of the specimen on the detector without any intervening lenses. This allows for a large field of view, limited by the size of the detector, while maintaining sub-micron resolution. Lensless microscopes are also cost effective, where the most expensive component is an image sensor costing a few dollars, and it allows for portability as there is no precise alignment needed. For certain applications, lensless microscopy may be more advantageous than the standard microscope. It is particularly well-suited to analysis applications in which a large quantity of specimens must be screened in order to determine whether a sample is positive or negative, for example in the case of the papanicolaou smear test for cervical cancer in which dysplastic cells are less than 1% [1]. Applications can be further extended to the determination of sperm motility [2] and blood cell counting [3]. Lensless microscopes are able to monitor cell division, motility, viability of biological samples, and can be placed within an incubator for extended cell studies. One of the major advantages of using lensless imaging is the adaptability and cost effectiveness allowing these devices to be implemented as point-of-care instruments for low-resource areas. Outside of medical diagnosis, it is also useful in air and water quality monitoring [4]; however, for the purposes of this thesis, the focus will remain on health care applications.

Lensless imaging can be used in combination with microfluidics to make a cost-effective and portable device that can evaluate milliliters of liquid for microscopic specimen. Microfluidics is the manipulation of sub-milliliter volumes of fluids, often used in biology and medical research. Studies in the field aim to replace traditional assays by decreasing the cost and while maintaining sensitivity, specificity, and throughput [5]. Microfluidics is used for the manipulation of single cells which could not otherwise be done. Microfluidic channels are used in combination with a conventional optical microscope to allow for the culture, analysis, and manipulation of cells in research or diagnostics [6][7]. By replacing glass slides with a microfluidic channel, a larger amount of fluid can be analyzed in a shorter amount of time. It can be combined with lensless imaging for a low-cost, high-throughput analysis device.

In the following chapter, I will be discussing three different lensless imaging approaches: shadow, fluorescence, and holographic imaging. Each technique can be adapted to fit their specific application. A technique known as pixel super resolution (PSR) is a post-processing imaging technique that is commonly used alongside holographic and shadow imaging to increase the resolution of the images, and will also be discussed in the coming sections.

3.1 Shadow Imaging

Shadow imaging, also known as projection imaging, is the most basic lens-free imaging setup. In this system a sample is placed immediately on top of an image sensor, and an incoherent light source, typically an LED, is placed above the sensor (Fig. 3.1). This allows the light to pass through the sample, become attenuated, and proceed to the detector, projecting an image of the sample. The sample can be imaged stained or unstained, and the images collected on the sensor exhibit a high level of complexity that allows pattern recognition algorithms to identify the specimens, in greyscale or colour. The resolution of the images attained from this modality is limited to twice the size of the pixel [1]. Current complementary metal-oxide semiconductors (CMOS) and charge-coupled devices (CCD) have pixel sizes ranging from $\sim 1\mu\text{m}$ to $\sim 10\mu\text{m}$. The size of the sensor can range from millimeters to centimeters in diameter, allowing for a large field of view. The parameters of the image sensor can vary with the application. For example, if the device will be used for the analysis of large particles in a microfluidic channel, a fast readout rate may take precedence over a small pixel size. More information on choosing an appropriate detector can be found in chapter 4.1.2.

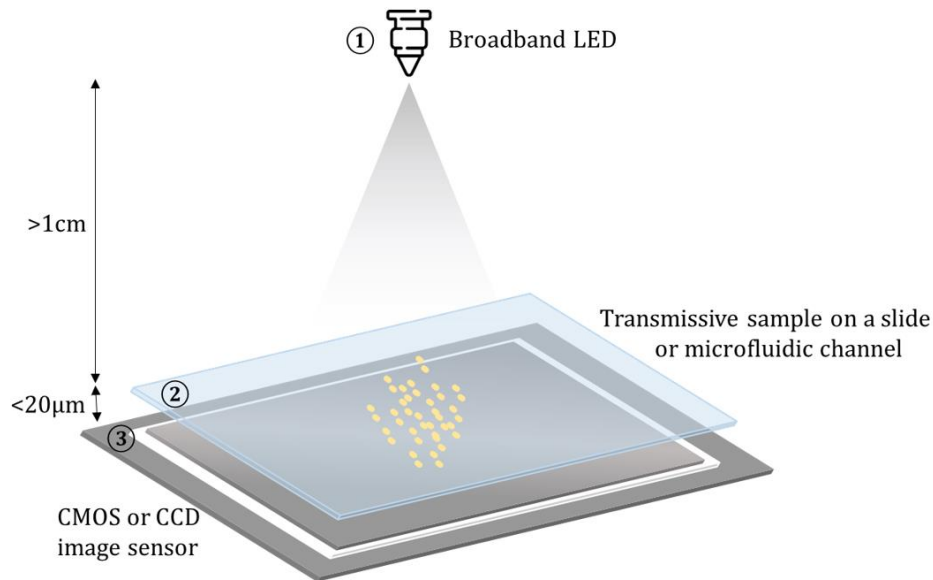


Figure 3.1: A Shadow Imaging Setup. A light source is placed several centimeters above the sample and detector. A transmissive sample is placed on the image sensor. The three main components are (1) an LED, (2) a sample holder, and (3) an image sensor.

The challenge in this setup is minimizing the distance between the sample and the sensor. In order to reduce the amount of diffraction and obtain a clear image, this distance can be no more than a few microns. The quality of the acquired image deteriorates severely with even the smallest increase in this parameter, which may be a challenging obstacle to overcome as most imaging sensors are made with a glass cover over the chip in order to protect the electronics and imaging chip. This glass cover can be removed and replaced with a thin PDMS membrane to preserve the imaging chip, however there have been procedures that forgo this step altogether and place the sample directly on the imaging pixels for the best possible resolution. With a delicate cleaning process, this sensor may be reusable [8]. In certain applications it is not necessary to obtain high-resolution images and sample-sensor minimization can be avoided. In these cases, the resolution of the sample is high enough such that a pattern recognition algorithm can be implemented and used to identify the sample, having been trained by learning algorithms for blood smear [9]. In other applications, where the primary goal is to determine the morphology of the sample, an aperture array can be used to increase the resolution of the image as it is now limited by the size of the aperture [10]. An important advantage of shadow imaging is that the images acquired do not require extensive post processing or reconstruction, however if a higher resolution is required, pixel super-resolution algorithms can be applied [11]. It is normally well suited for the imaging of biological specimen, in which the samples have some degree of transparency.

A simple shadow imaging device named LUCAS was developed in 2007 by the Ozcan group [12]. This device was developed as a diagnostic point-of-care (POC) device for HIV monitoring in developing countries. By implementing a microfluidic device controlling blood flow over the image sensor, the device was able to capture and count cells from whole blood to achieve a high-throughput count over a large field of view. There have been numerous adaptations and improvements over the years. Better commercial image sensors were able to increase the raw resolution of the images, and the implementation of pixel super-resolution algorithms is now routine. With these improvements, Yang et al. achieved a resolution of 660nm in adherent cell culture and in other POC devices [11][8]. They also implemented microfluidic attachments to analyze cells flowing through channels (Fig. 3.2) [13]. Proof-of-concept experiments with lensless shadow imaging have been done with microbeads and cultured biological specimen, as well as diluted whole blood samples. A super-resolution microfluidic hemocytometer has been developed on a CMOS sensor with a 1.1 μm pixel pitch, on which diluted whole blood flows through the microfluidic channel at a flow rate of 5 $\mu\text{l}/\text{min}$ by syringe pumping. Red blood cells (8 μm), white blood cells (12 μm) and platelets (2 μm) were recognized by feature shape and size [14]. Complete blood cell counting is an application that can benefit from the use of a point-of-care device. Shadow imaging devices for waterborne parasite identification [15] and long term motility [16] and growth [17] of microorganisms have also been developed.

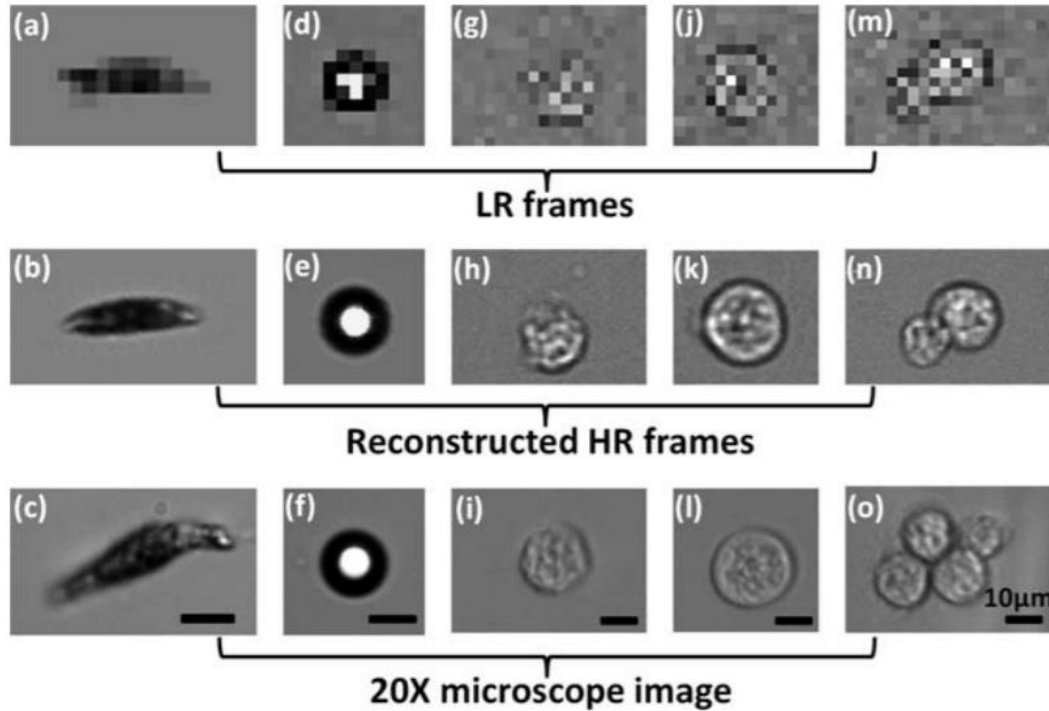


Fig. 3.2: Shadow images of *Euglena gracilis* (a–c), microspheres (d–f), and *Entamoeba invadens* cysts (g–o). The LR frames (top row) are directly from the device, with reconstructed HR frames below. Brightfield microscopy images taken with 20x objective lens are on the bottom row. Figure and caption derived from Zheng et al. [13] G. Zheng, S. A. Lee, S. Yang, and C. Yang, “Sub-pixel resolving optofluidic microscope for on-chip cell imaging,” *Lab Chip*, vol. 10, no. 22, p. 3125, Oct. 2010.- Reproduced by permission of The Royal Society of Chemistry

3.2 Fluorescence lensless imaging

Fluorescence imaging is one of many microscopic techniques that has been adapted to be lens-free. Fluorescence microscopy is often the gold standard for biomedical and clinical research; however, its use beyond established laboratories is limited due to the bulky and expensive setups. A lensless fluorescent imaging device can be integrated into automated systems aimed at providing high-throughput biological and medical screening. This is due to their large field of view, compact and cost effective hardware, and simple usability [18].

In a lensless setup, similar to the conventional fluorescence microscope, there is an excitation light source which excites the sample. The sample emits the light at a longer wavelength, and the image sensor collects the emission light. If the sensor is sensitive to the excitation light, as it normally is, a filter must be placed between the sample and the sensor to reject the wavelength. The setup for lensless fluorescent imaging is similar in structure to that of shadow imaging with the exception of this emission filter. In a direct imaging setup like this one, the excitation light remains a concern as the ratio between the signal and background light is quite low. Other

components can be added to the system to achieve a better signal to noise ratio, such as a glass spacer to reject a part of the excitation light through total internal reflection [12].

Achieving a high spatial resolution is the main difficulty of this technique. The resolution of fluorescence imaging is limited by its point spread function (PSF), which is the spot on the sensor that is recorded from one point on the sample. In a lensless modality, the PSF increases with an increase in sample-to-sensor distance. For example, for a sample-to-sensor distance of $\sim 200\mu\text{m}$, the PSF will be $\sim 200\mu\text{m}$ [19]. A distance of $200\mu\text{m}$ is usually necessary in order to implement a filter to reject the excitation light from entering the imaging sensor. Despite this caveat, there exists hardware and computational approaches to increase the resolution, for instance integrating a filter directly into the image sensor such that the sample-to-sensor distance is minimized. With this approach, a spatial resolution of approximately $\sim 13\mu\text{m}$ has been achieved [20]. A tightly packed array of tapered optical fibers can also be integrated into the system to relay the fluorescence emission from the sample to the sensor, moderately magnifying the image, increasing the resolution to $4\mu\text{m}$ [21]. Recently, a fluorescence microscope called the FlatScope has achieved a lateral resolution of $2\mu\text{m}$ by placing an amplitude mask $200\mu\text{m}$ above the imaging sensor and implementing a reconstruction algorithm (Fig. 3.3) [22].

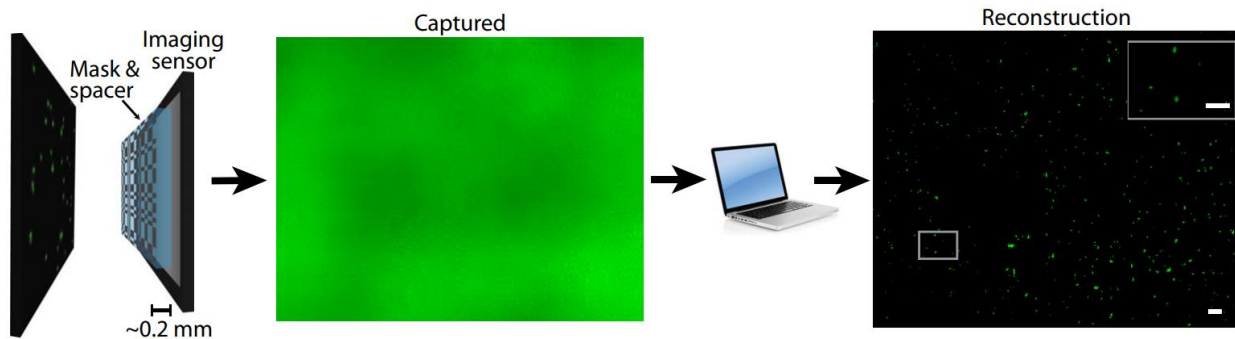


*Figure 3.3: FlatScope setup. The FlatScope consists of an amplitude mask and $200\mu\text{m}$ spacer placed above an absorptive gel filter (not shown). The device is less than 1mm thick. A reconstruction algorithm is implemented to recover a high resolution image of the sample [22]. Reprinted from [J. K. Adams et al., “Single-frame 3D fluorescence microscopy with ultraminiature lensless FlatScope,” *Sci. Adv.*, vol. 3, no. 12, p. e1701548, Dec. 2017]. © The Authors, some rights reserved; exclusive licensee American Association for the Advancement of Science. Distributed under a Creative Commons Attribution NonCommercial License 4.0 (CC BY-NC) <http://creativecommons.org/licenses/by-nc/4.0/>*

A number of lensless fluorescence devices have been developed for biological research. A particularly suited application for lensless fluorescent microscopy is implantable devices for live brain imaging in rodents as it is small and lightweight, allowing for deep brain imaging [23]. In these cases, memory, learning, and behavioural studies can be carried out on rodents without the need to tether the rodent to a microscope, allowing for freely moving conditions [24].

3.3 Holographic lensless imaging

Holographic lensless imaging is very similar in setup to shadow imaging. The main differences are the type of light source used and the distance between the sample and the detector. An optically coherent light source, which can be produced by placing a small pinhole in front of an LED, is used [1]. As well, the distance between the sample and the sensor is enlarged to around a centimeter. Both of these adjustments result in a diffraction image being produced on the sensor.

Holographic lensless imaging is an application of digital in-line holography, and is an adaptation of conventional brightfield imaging. Traditional holography requires two coherent light beams to produce a hologram, the reference beam and the object beam (Fig. 3.4a). In standard, off-axis holography, the two beams are separated and take different paths through an interferometer. The object beam passes through the object container accumulating some phase difference before recombination with the reference arm and before hitting the detector. Together the initial coherence condition and the optical path difference from the sample produce interference which is displayed on the detector as an interference pattern. In digital in-line holography, the two light waves share the same optical axis (Fig. 3.4b). The reference wave is light which passes unscattered through the sample. The object wave is produced from light scattered by the sample. The two waves interfere with one another before creating an interference pattern, allowing the detector to record the interference pattern. This interference pattern carries information that can be used to reconstruct the image at the object plane. Holographic reconstruction consists of two parts. First, the light intensity recorded on the detector is back-propagated to the object plane. In in-line holography, this recovered image is strongly affected by an artifact known as the “twin image” due to the lack of phase information in the acquisition process. This twin image is due to the geometry of the setup; because the light is being propagated over one axis, the real and virtual image appear overlapping on the detector. This leads to the second step in the reconstruction, phase retrieval. This part of the reconstruction recovers the image without the presence of the twin image [6].

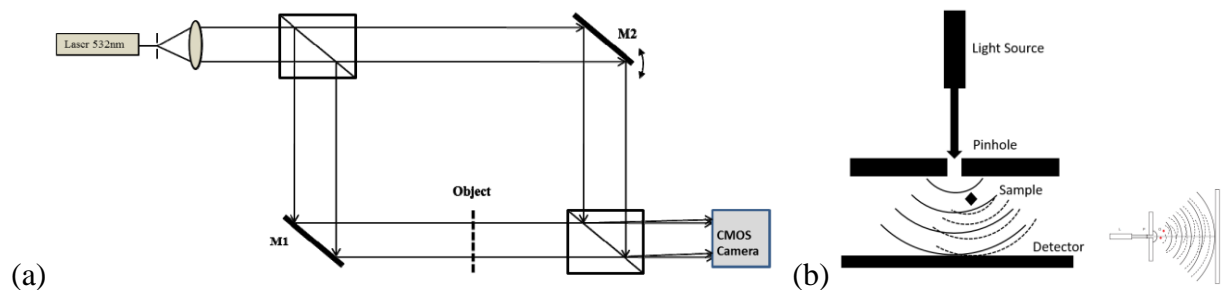


Figure 3.4: (a) Off-axis holography with a Mach-Zehnder interferometer demonstrating the object and reference beam separation and recombination before their detection. Samples within the object arm will produce interference upon recombination with the reference arm; Reprinted with permission from [25] © The Optical Society. (b) In-line holography demonstrating the interference effects from samples within the propagation space [26]. A light source (L) is shone through a pinhole (P). A spherical wave emerges (solid line) and passes around and through the

objects (O) creating scattered waves (dashed lines). The scattered waves will interact with the reference waves and interfere creating interference patterns at the detector.

3.3.1 Back Propagation

The first component of the reconstruction is back propagation. This part of the reconstruction is highly dependent on the setup used to create the diffraction pattern, as it is a model of the propagating light through the setup. If the setup changes, so does the propagation of the light. The type of light waves, the distance between the sample and the detector, and the positions of the object and reference beams all contribute to the model. The addition of lenses also increases the complexity in modeling wavefront propagation, though they are omitted in this setup. The typical setup of an in-line lensless holographic imaging device is shown in Fig. 2b. In this digital in-line system, light propagates from the source and passes through a sample that is a short distance away from a digital detector. Because the distance between the sample and the light source is much larger than the distance between the sample and the detector, the incident wave can be considered a plane wave between the sample and the sensor [1]. In which case, plane wave reconstruction, as opposed to reconstruction from spherical waves, can be carried out. If the distance between the sample and the detector is small, the Fresnel approximation can be used, and if this distance is large, the Fraunhofer estimation is used. The Fresnel approximation is primarily used in lensless holographic imaging.

At the sample plane, where the incident light wave interacts with the sample (x_s, y_s) , the electric field is described as the sum of the reference wave and the object wave at the sample:

$$E_s = E_{R,s} + E_{O,s} = A_R + A_O(x_s, y_s)e^{i\phi_O(x_s, y_s)},$$

A_R is the amplitude of the plane reference wave, which is spatially uniform, as it is not perturbed by the sample. $A_O(x_s, y_s)$ is the spatially varying amplitude of the object, which perturbs the light as it passes through. It is also defined as the transmittance of the object. $\phi_O(x_s, y_s)$ is the spatially varying phase, or optical thickness, of the object. The goal of holographic reconstruction is to determine A_O and ϕ_O at the object plane from the acquisition of the light intensity of the interference pattern at the sensor [1].

There are three main methods for modeling the propagation of waves between parallel planes in order to reconstruct the hologram at the object plane once Fresnel diffraction has been established. These methods are the Fourier transform based Fresnel method, the convolution based Fresnel method, and the angular spectrum method. A thorough analysis on the different methods can be found here [27]. Though all three approaches are acceptable and have been shown to be valid in lensless systems, the angular spectrum approach is accepted as it works for small propagation distances and does not use paraxial approximations [28]. It also has the benefit of being more intuitive and free from boundary conditions leading to a more robust calculation of diffraction [29].

Unfortunately, a caveat of using inline holography is the presence of a twin image artifact, thus, after determining an appropriate model for the light propagation in the system, phase recovery is needed in order to eliminate the twin image artifact. Under different circumstances, such as off-axis holography, the detector records an interference pattern between the object wave and the reference wave. However, in inline holography, where a clean reference wave is not present, the recording is more generally assumed to be a diffraction pattern. Under this condition, the optical phase cannot be inferred from a single measurement, unless additional assumptions are made, and known information is enforced.

3.3.2 Phase Retrieval

One method of phase determination and simultaneous twin-image removal is by computationally propagating the optical field back and forth between the sensor plane and the object plane, enforcing known information at each plane [1]. This technique incorporates a whole class of phase recovery algorithms originating from the Gerchberg–Saxton algorithm. The known information at the sensor plane is the amplitude of the optical field, which is simply the captured intensity image of the diffraction patterns. At the sample plane, an assumption is made that outside of the boundaries of the individual objects, the amplitude and phase of the light is uniform [1]. This assumption is generally only enforced for sparse samples. After applying several iterations of the phase recovery algorithms, the reconstruction of the optical field converges to a physically consistent function and the twin image artifacts are eliminated. In order for this technique to be successful, the boundaries of the objects in the image must be well defined, which might not always be easily done in an automated fashion [1].

Another method of phase retrieval, which can be applied to more dense samples, is based on imaging the sample at varying distances from the detector. This approach is incorporated within the class of algorithms mentioned above as it also involves computationally propagating the optical field back and forth between the sensor plane and the object plane, enforcing known information at each plane [30]. As there is a greater amount of sampling, there are more knowns.

3.3.3 Digital In-line Holography as a Lensless Imaging Technique

In building a digital inline holographic device, there is no hard limit in distancing the light source, sample, and detector, which allows for a multitude of variations to be made to the device, unlike in shadow imaging. Holography also allows for 3D reconstruction of the sample as reconstruction through back propagation can be done at numerous z distances through the sample. As well, digital holographic reconstruction in combination with additional techniques allow for great resolving power. Lensless holography is limited by the size of the pixels on the detector, where the resolution of the reconstructed hologram is twice that of the pixel size, however, efforts to increase this resolution has led to the application of pixel super resolution algorithms which are applied to the low resolution hologram prior to reconstruction. In combination with pixel super resolution (PSR), a resolution of $\sim 0.6\mu\text{m}$ has been achieved [31]. With PSR algorithms and a UV wavelength of 372nm, gratings with a 225nm half-pitch have been resolved [32]. In combination with self-assembled nanolenses on the surface of the image

sensor, a resolution of 40nm has been achieved. Though these resolutions are possible, the methods to achieve the resolutions are exploratory. Holographic reconstruction in combination with PSR requires a lot of computational power, which means it may not yet be suited for real-time readouts. In addition, the setup and reconstruction of holographic imaging is interdependent and there are numerous limitations and challenges in a typical system, such as sample sparsity, twin image artifact removal, colour imaging. Though most of these limitations can be overcome, it is at no superficial computational cost. Despite the drawbacks, numerous diagnostic tools have been made using this technique, many of them portable and capable of remote testing.

Though a detailed review of the applications of lensless digital holography is beyond the scope of this review, a number of devices have been fabricated as an alternative to standardized health care screens. These include blood counting and analysis [33], pap smear analysis [34], sperm motility analysis (Fig. 3.5) [35], and so on. Others have been fabricated for water and air testing [36].

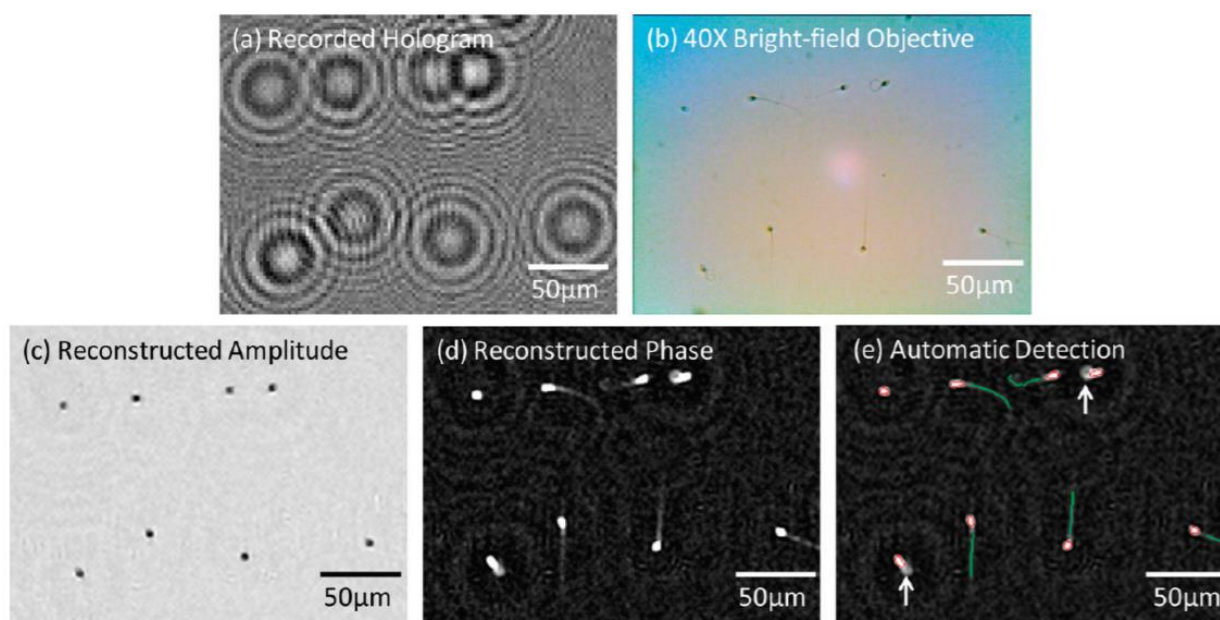


*Figure 3.5: (a) Lensfree hologram of an immobilized semen sample (b) A bright-field microscope image of the same FOV as in (a) 40× objective-lens; NA: 0.65. (c,d) The reconstructed amplitude and phase images from (a). (e) Automatic detection of the sperm. Figure and caption derived from Su et al. [35] Reprinted with permission from (T.-W. Su, A. Erlinger, D. Tseng, and A. Ozcan, “Compact and Light-Weight Automated Semen Analysis Platform Using Lensfree on-Chip Microscopy,” *Anal. Chem.*, vol. 82, no. 19, pp. 8307–8312, Oct. 2010). Copyright (2019) American Chemical Society.*

3.4 Pixel Super Resolution

Depending on the application, lensless imaging may not be a viable imaging method due to its low resolution, normally limited to the size of a pixel without computational intervention.

Research on the development of different lensless imaging devices normally fall into two categories, one being a resolution increase, and the other being a change in modality (ie. Phase contrast imaging, DIC, confocal, etc.). In order to increase the resolution, pixel super-resolution is commonly employed, and although it is often used in this field, the applications are endless. Digital imaging is widely used to gather qualitative and quantitative results. As a result, high quality images are often required. At times, the instrumentation of the imaging devices is limited in its quality, either due to physical/mechanical limitations, cost, or time. In order to improve image quality without changing the instrumentation, one may implement post-processing on the images. In this chapter, the advantage of pixel super-resolution (PSR) on imaging is discussed.

PSR is an image processing technique which works to increase the resolution of an image. It is the process through which a low-resolution (LR) image, or a set of low-resolution images, are used to create a single high-resolution (HR) image[37]. There are a number of PSR techniques that have been implemented to do this, ranging from frequency to spatial domain approaches, and signal processing to machine learning perspectives. Example-based and multiframe PSR are common techniques applied to lensless holographic and shadow imaging to increase the resolution of the acquired images. In example-based PSR, a neural network is trained by a series of patches from HR images and then fed a LR image. The algorithm then creates an HR image from the LR input. In multiframe PSR, an HR image is reconstructed from a series of sub-pixel shifted LR images through the extraction of non-redundant information (Fig. 3.6). This increases the high frequency components of the image and reduces the degradations of a low-resolution camera[37].

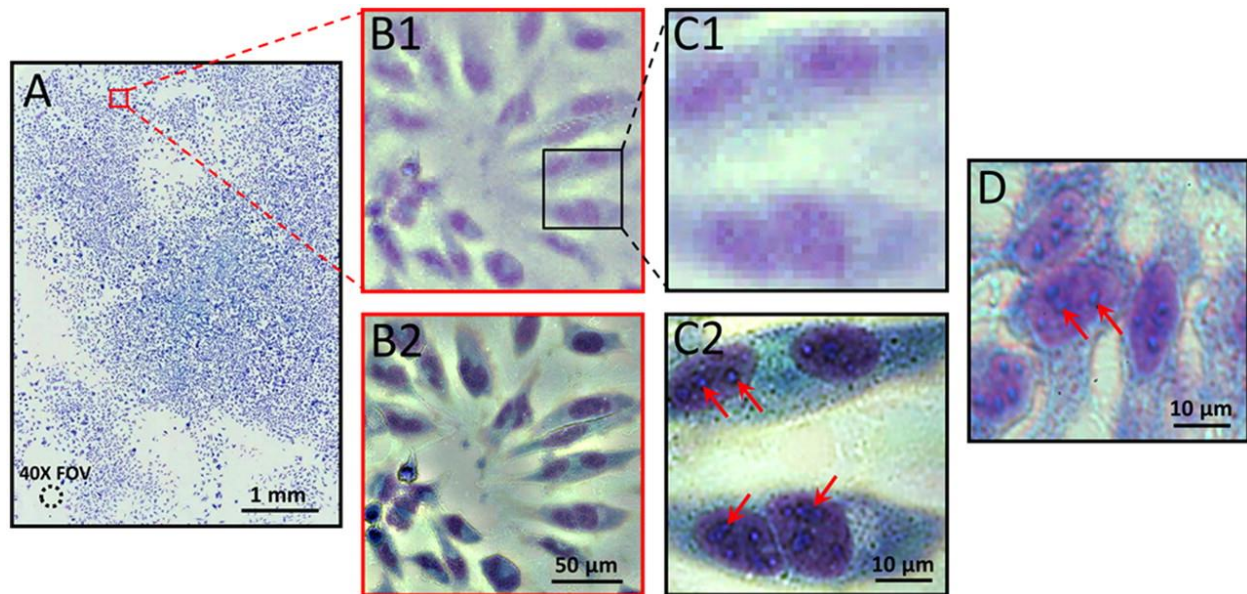


Figure 3.6: (A) Confluent HeLa cell sample (B1 and C1) Raw images of a small region of A. (B2 and C2) The reconstructed high-resolution images corresponding to B1 and C1. (D) The conventional microscopy image, with 40× objective lens (0.66 N.A.). Figure and caption from Zheng et al. [11]

3.4.1 PSR in Optofluidics

PSR has been used to improve the resolution of several lensless imaging devices. Multiframe super-resolution requires that there are multiple sub-pixel shifted images in order to reconstruct an HR image. This can be done by shifting the light source above a sample [11], or shifting the sample itself, for instance through a microfluidic channel [13]. By shifting the light source in a precise manner, it is possible to very accurately reconstruct the HR image because the exact sub-pixel shift between the images is known. The same holds true for a controlled stage that is shifting a sample. As for optofluidic devices where there is flow through a channel, it is more difficult to model the motion of the particles within the channel and register the images to one another. If multiple cells are within the channel, the motion becomes complex and registration becomes more difficult. This also holds true if there are different type of motion within the channel, like rolling, tumbling, obstructed flow. Current registration techniques are developing the ability to register images with complex movement.

Example based PSR is able to capture a single frame of the flowing cells and resolve it based on the high resolution images that were used to train it [14][38]. Although more convenient, the HR images in this case are “hallucinated” images of the real sample. Through rigorous training, the images may be more representative of the truth.

3.5 Commercial Devices

The iPARSENS is a commercial lensless imaging device targeted toward researchers culturing cells; however, to our knowledge, there have been no commercial devices with lensless imaging technology in health care. This may be for several reasons. First, the computation time for many classification and reconstruction algorithms may be too slow, and it is too costly to increase this processing time. Holographic reconstruction algorithms are time consuming and rigorous on computational devices. There have been impressive devices that have been made on a low budget, however, now there requires a shift from cost effectiveness to ease-of-use, rapid throughput and portability. Secondly, optofluidic devices require a microfluidic pump to flow the fluids through the microfluidic channel and over the sensor, which are typically bulky, and large. Low-cost devices may also have a shorter life span and cannot yet replace equipment that is more robust [39]. Lastly, the testing of novel medical devices is lengthy and challenging. After development, there should be a pilot study to investigate the benefit of using the lensless device in a clinical setting.

3.6 Optical Devices for Urinalysis

Recently, Zhang et al. developed a lensless holographic imaging device for the analysis of parasites in cerebrospinal fluid [40]. Their device is adaptable to *Trichomonas vaginalis* detection, though further testing must be done in spiked urine samples. The device uses holographic phase imaging to scan and analyze 3ml of fluid in 20 minutes. The limit of detection was found to be 10 parasites per milliliter of whole blood, and it costs ~\$1850 USD to construct one device. This cost does not include the price of a high-end laptop which is necessary for the short processing time. Schroder et al. developed a device that traps bacteria in an array of

geometrical traps and optically analyzes them through Raman spectroscopy. It can analyze bacteria from urine samples without prior preparation steps in under 70 min [41]. The advantage of this technique is the ability to discern different strains of bacteria in a short amount of time. Optical devices for urinalysis have the potential to detect and analyze different components of urine, thus allowing for a universal testing platform.

3.7 Discussion and Conclusion

The lensless imaging devices discussed in this chapter have their own advantages and disadvantages which should be taken into consideration when choosing an application. One method is not objectively better or worse than another, simply more or less suited for a task. The application we are interested in is urine analysis.

Fluorescence imaging of a sample requires it to fluoresce, either through autofluorescence or after being stained with a fluorophore. In the case of urinalysis, minimal sample preparation would be beneficial to the cost and turnover time, indicating that the addition of fluorophores should be avoided if possible. Analyzing the autofluorescence of urine is possible, however it is a highly complex mosaic of microparticles and metabolites [42].

Lensless holographic imaging has shown great promise in sample analysis. Benefits to holographic imaging include 3D reconstruction and a less stringent sensor-sample distance. Holography also allows for phase recovery of the sample which may be of benefit to imaging bacteria. Although bacteria are transparent and do not significantly affect the intensity of light that pass through them, the phase of the light is affected. Despite these advantages, holographic imaging requires intensive post-processing of the images. In this case, there may be a need for longer processing times, or a more expensive computer [40].

Shadow imaging does not require image reconstruction and it is able to attain the same resolution as holographic imaging; however it is difficult to attain a very small sensor-sample distance. For urinalysis there is no need for 3D reconstruction, and the components of urine are uniquely identifiable by their morphology.

The next chapter outlines the design, fabrication, and characterization of a lensless shadow imaging device for urine analysis.

References

- [1] A. Ozcan and E. McLeod, “Lensless Imaging and Sensing,” *Annu. Rev. Biomed. Eng.*, vol. 18, no. 1, pp. 77–102, Jul. 2016.
- [2] T.-W. Su, I. Choi, J. Feng, K. Huang, E. McLeod, and A. Ozcan, “Sperm Trajectories Form Chiral Ribbons,” *Sci. Rep.*, vol. 3, no. 1, p. 1664, Dec. 2013.
- [3] S. A. Arpali, C. Arpali, A. F. Coskun, H.-H. Chiang, and A. Ozcan, “High-throughput screening of large volumes of whole blood using structured illumination and fluorescent

- on-chip imaging,” *Lab Chip*, vol. 12, no. 23, p. 4968, Dec. 2012.
- [4] Y. Wu and A. Ozcan, “Lensless digital holographic microscopy and its applications in biomedicine and environmental monitoring,” *Methods*, vol. 136, pp. 4–16, Mar. 2018.
- [5] E. K. Sackmann, A. L. Fulton, and D. J. Beebe, “The present and future role of microfluidics in biomedical research,” *Nature*, vol. 507, no. 7491, pp. 181–189, Mar. 2014.
- [6] R. Delacroix *et al.*, “Cerebrospinal fluid lens-free microscopy: a new tool for the laboratory diagnosis of meningitis,” *Sci. Rep.*, vol. 7, p. 39893, Jan. 2017.
- [7] F. Ellett *et al.*, “Diagnosis of sepsis from a drop of blood by measurement of spontaneous neutrophil motility in a microfluidic assay,” *Nat. Biomed. Eng.*, vol. 2, no. 4, pp. 207–214, Apr. 2018.
- [8] S. A. Lee and C. Yang, “A smartphone-based chip-scale microscope using ambient illumination,” *Lab Chip*, vol. 14, no. 16, pp. 3056–3063, Jul. 2014.
- [9] Y. Fang, N. Yu, R. Wang, and D. Su, “An on-chip instrument for white blood cells classification based on a lens-less shadow imaging technique,” *PLoS One*, vol. 12, no. 3, p. e0174580, Mar. 2017.
- [10] X. Cui *et al.*, “Lensless high-resolution on-chip optofluidic microscopes for *Caenorhabditis elegans* and cell imaging,” *Proc. Natl. Acad. Sci. U. S. A.*, vol. 105, no. 31, pp. 10670–5, Aug. 2008.
- [11] G. Zheng, S. A. Lee, Y. Antebi, M. B. Elowitz, and C. Yang, “The ePetri dish, an on-chip cell imaging platform based on subpixel perspective sweeping microscopy (SPSM),” *Proc. Natl. Acad. Sci. U. S. A.*, vol. 108, no. 41, pp. 16889–94, Oct. 2011.
- [12] A. F. Coskun, T.-W. Su, and A. Ozcan, “Wide field-of-view lens-free fluorescent imaging on a chip,” *Lab Chip*, vol. 10, no. 7, pp. 824–7, Apr. 2010.
- [13] G. Zheng, S. A. Lee, S. Yang, and C. Yang, “Sub-pixel resolving optofluidic microscope for on-chip cell imaging,” *Lab Chip*, vol. 10, no. 22, p. 3125, Oct. 2010.
- [14] X. Liu *et al.*, “A Microfluidic Cytometer for Complete Blood Count With a 3.2-Megapixel, 1.1- μm -Pitch Super-Resolution Image Sensor in 65-nm BSI CMOS,” *IEEE Trans. Biomed. Circuits Syst.*, vol. 11, no. 4, pp. 794–803, Aug. 2017.
- [15] S. A. Lee *et al.*, “Imaging and Identification of Waterborne Parasites Using a Chip-Scale Microscope,” *PLoS One*, vol. 9, no. 2, p. e89712, Feb. 2014.
- [16] S. A. Lee, G. Zheng, N. Mukherjee, and C. Yang, “On-chip continuous monitoring of motile microorganisms on an ePetri platform,” *Lab Chip*, vol. 12, no. 13, pp. 2385–90, Jul. 2012.
- [17] J. H. Jung and J. E. Lee, “Real-time bacterial microcolony counting using on-chip microscopy,” *Sci. Rep.*, vol. 6, p. 21473, Feb. 2016.
- [18] H. Takehara *et al.*, “On-chip cell analysis platform: Implementation of contact fluorescence microscopy in microfluidic chips,” *AIP Adv.*, vol. 7, no. 9, p. 095213, Sep.

- 2017.
- [19] A. F. Coskun, T.-W. Su, and A. Ozcan, “Wide field-of-view lens-free fluorescent imaging on a chip.,” *Lab Chip*, vol. 10, no. 7, pp. 824–7, Apr. 2010.
 - [20] S. Ah Lee, X. Ou, J. E. Lee, and C. Yang, “Chip-scale fluorescence microscope based on a silo-filter complementary metal-oxide semiconductor image sensor.,” *Opt. Lett.*, vol. 38, no. 11, pp. 1817–9, Jun. 2013.
 - [21] A. F. Coskun, I. Sencan, T.-W. Su, and A. Ozcan, “Wide-field lensless fluorescent microscopy using a tapered fiber-optic faceplate on a chip.,” *Analyst*, vol. 136, no. 17, pp. 3512–8, Sep. 2011.
 - [22] J. K. Adams *et al.*, “Single-frame 3D fluorescence microscopy with ultraminiature lensless FlatScope,” *Sci. Adv.*, vol. 3, no. 12, p. e1701548, Dec. 2017.
 - [23] J. Ohta *et al.*, “Implantable Microimaging Device for Observing Brain Activities of Rodents,” *Proc. IEEE*, vol. 105, no. 1, pp. 158–166, Jan. 2017.
 - [24] T. Kobayashi *et al.*, “Novel implantable imaging system for enabling simultaneous multiplanar and multipoint analysis for fluorescence potentiometry in the visual cortex,” *Biosens. Bioelectron.*, vol. 38, no. 1, pp. 321–330, Oct. 2012.
 - [25] K. Khare, P. T. S. Ali, and J. Joseph, “Single shot high resolution digital holography,” *Opt. Express*, vol. 21, no. 3, p. 2581, Feb. 2013.
 - [26] B. S. Nickerson and H. J. Kreuzer, “Deconvolution for digital in-line holographic microscopy,” *Adv. Opt. Technol.*, vol. 2, no. 4, pp. 337–344, Jan. 2013.
 - [27] T. Latychevskaia and H.-W. Fink, “Practical algorithms for simulation and reconstruction of digital in-line holograms,” *Appl. Opt.*, vol. 54, no. 9, p. 2424, Mar. 2015.
 - [28] Z. Göröcs, L. Orzó, M. Kiss, V. Tóth, and S. Tőkés, “In-line color digital holographic microscope for water quality measurements,” 2010, p. 737614.
 - [29] M. K. Kim, *Digital holographic microscopy: principles, techniques, and applications*. Springer, 2011.
 - [30] O. Mudanyali *et al.*, “Compact, light-weight and cost-effective microscope based on lensless incoherent holography for telemedicine applications,” *Lab Chip*, vol. 10, no. 11, p. 1417, 2010.
 - [31] W. Bishara, T.-W. Su, A. F. Coskun, and A. Ozcan, “Lensfree on-chip microscopy over a wide field-of-view using pixel super-resolution.,” *Opt. Express*, vol. 18, no. 11, pp. 11181–91, May 2010.
 - [32] A. Greenbaum, W. Luo, B. Khademhosseini, T.-W. Su, A. F. Coskun, and A. Ozcan, “Increased space-bandwidth product in pixel super-resolved lensfree on-chip microscopy,” *Sci. Rep.*, vol. 3, no. 1, p. 1717, Dec. 2013.
 - [33] S. Seo *et al.*, “Lensfree holographic imaging for on-chip cytometry and diagnostics,” *Lab Chip*, vol. 9, no. 6, pp. 777–787, 2009.

- [34] W. Luo, Y. Zhang, A. Feizi, Z. Göröcs, and A. Ozcan, “Pixel super-resolution using wavelength scanning,” *Light Sci. Appl.*, vol. 5, no. 4, pp. e16060–e16060, Apr. 2016.
- [35] T.-W. Su, A. Erlinger, D. Tseng, and A. Ozcan, “Compact and Light-Weight Automated Semen Analysis Platform Using Lensfree on-Chip Microscopy,” *Anal. Chem.*, vol. 82, no. 19, pp. 8307–8312, Oct. 2010.
- [36] Y.-C. Wu *et al.*, “Air quality monitoring using mobile microscopy and machine learning,” *Light Sci. Appl.*, vol. 6, no. 9, p. e17046, Sep. 2017.
- [37] P. Milanfar, *Super-resolution imaging*. CRC Press, 2011.
- [38] X. Huang *et al.*, “Machine Learning Based Single-Frame Super-Resolution Processing for Lensless Blood Cell Counting,” *Sensors*, vol. 16, no. 11, p. 1836, Nov. 2016.
- [39] J. Rajchgot *et al.*, “Mobile-phone and handheld microscopy for neglected tropical diseases,” *PLoS Negl. Trop. Dis.*, vol. 11, no. 7, p. e0005550, Jul. 2017.
- [40] Y. Zhang *et al.*, “Motility-based label-free detection of parasites in bodily fluids using holographic speckle analysis and deep learning,” *Light Sci. Appl.*, vol. 7, no. 1, p. 108, Dec. 2018.
- [41] U.-C. Schröder *et al.*, “Rapid, culture-independent, optical diagnostics of centrifugally captured bacteria from urine samples.,” *Biomicrofluidics*, vol. 9, no. 4, p. 044118, Jul. 2015.
- [42] M. Zvarik, D. Martinicky, L. Hunakova, I. Lajdova, And L. Sikurova, “Fluorescence characteristics of human urine from normal individuals and ovarian cancer patients,” *Neoplasma*, vol. 60, no. 05, pp. 533–537, 2013.

Chapter 4.

Device Design, Fabrication, and Characterization

The previous chapters discussed the importance of urinalysis, the difficulties of existing urinalysis techniques, and the advantages of using lensless microscopy in health care platforms. Although urinalysis is a valuable routine medical diagnostic test, it results in high healthcare costs due to the volume of samples collected and screened. There would be a significant benefit to patients and the health care system if the number of samples and their turnaround time were reduced. This thesis aims to demonstrate that with appropriate adaptations, a point of care lensless optofluidic device can be developed to detect small particles in urine and contribute to patient diagnosis. This chapter covers the design and characterization of a lensless optofluidic device.

4.1 Development of a Urinalysis POC Device

The lensless imaging device we chose to fabricate is the shadow imaging platform. Of the three categories of lensless imaging, this one was the most suitable for our application. Alternatively, fluorescence imaging or holographic imaging may be used in lensless imaging applications. Fluorescence imaging would require a fluorescent stain to be added to the urine samples which would add a step in the processing. The type of stain would also have to be investigated as they are not universal and there are numerous components of urine. Holographic imaging requires intensive post-processing of the images and does not seem to offer any significant advantage over shadow imaging for our intended application. Perhaps after the development of a shadow imaging platform, holographic and fluorescence platforms can be investigated as alternative techniques.

The shadow imaging device presented in this thesis is composed of a light source, an image sensor, and a microfluidic channel. The microfluidic channel is placed in direct contact with an image sensor. These two components are clamped together by way of C-clamps with a glass slide on top of the channel and a holder below the sensor (Fig. 4.1). This “sandwich” configuration minimizes the sample-sensor distance by ensuring the channel is in direct contact with the sensor. The sensor’s holder has a divot to hold the sensor in place and supports the microfluidic channel by providing a flat surface on top of which the sample is allowed to flow. A broadband white light source is placed ~30cm above the setup. The following chapter will outline the ideal build for the device, the prototypes through which the final design was chosen, and the protocol through which it was made.

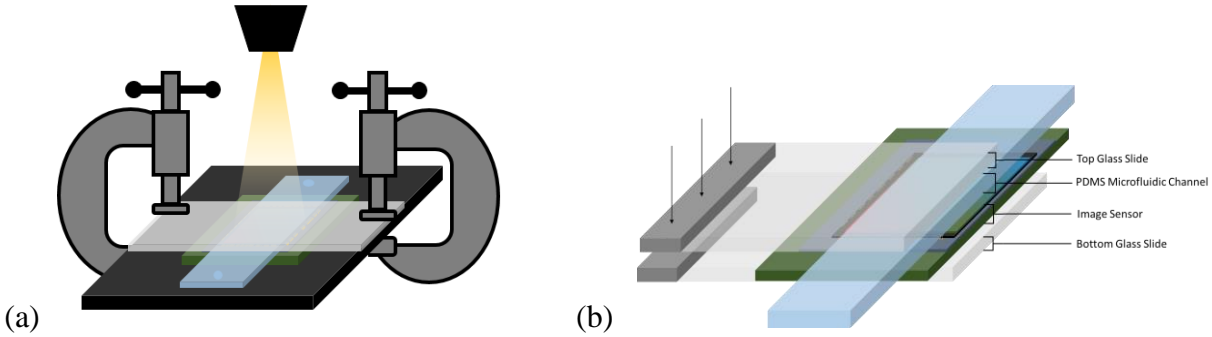


Figure 4.1: (a) Optofluidic shadow imaging setup. Two adjustable C-clamps squeeze the microfluidic channel to the image sensor. (b) The sensor and channel are placed between a sensor holder and a transparent glass slide. This pressure is required to hold the channel flush and steady against the sensor, and the glass allows for the light to pass through to the channel. The distance between the light source and the detector is much larger (~30cm) than the distance between the sample and the detector (direct contact).

4.1.1 Light Source

The light source that is used in shadow imaging is broadband and incoherent. A monochromatic coherent light source is used in holography to create a diffraction pattern around the cells, however in shadow imaging the goal is to have a clear image without reconstruction. The device must also only have one light source to illuminate the sample a constant distance above the sensor. If the light source moves, the samples on the sensor will also appear to move. If there are multiple light sources, such as fluorescent lighting in a room, the sample can cast multiple shadows per particle which results in an unclear image. Thus, a single LED is used to illuminate the sample. The distance between the LED and the sensor depends on the power of the LED and the quantum efficiency of the sensor. If the LED is too bright and too close, the sensor's pixels will oversaturate. If it is too dull or too far away, the recorded image will be too dark or not enough detail will be seen. In order to reduce the size of the device, a less powerful LED can be placed close to the sample. Other camera setting, such as ISO, framerate and exposure time can be adjusted to accommodate difference light source to samples differences. By lowering the ISO the camera is less sensitive to light. The sun on a clear day has also been used as a light source for previous devices to eliminate the need for a powered light source [1].

The light illuminating our platform originates from an incoherent 1W LED placed 30cm above the sample. The lamp (Ikea, product number 003.859.41) faces vertically downwards, directly over the image sensor and the diameter of the area of illumination is ~30cm (Fig. 4.2).



Figure 4.2: Simple LED lamp used as the incoherent broadband light source (Ikea, 003.859.41)

4.1.2 Detector

The detector in a lensless imaging device can vary greatly in its features. The resolution of the device is directly correlated to the size of the pixels on the detector. This is due to the fact that there are no magnifying lenses that are placed between the sample and the detector to enlarge the image of the sample before projecting it onto the detector. Each pixel lies beneath a part of the sample; if the sample is smaller than the pixel, it will be detected with no defining characteristics. The smallest pixel size commercially available is $\sim 1\mu\text{m}$ [2].

The field of view of the detector contributes to how much of the sample you can see at a time. Having a large field of view can be highly beneficial if the samples being analyzed are fixed, that way the entire sample can be imaged at once. A smaller field of view is not ideal as the sample would need to be scanned and the images stitched together. If the sample is flowing through a microfluidic channel, a large field of view can be sacrificed for a faster frame rate. Smaller detectors can acquire images at a greater speed, and the frame rate can be synchronized with the flow rate through the channel. A faster frame rate allows for a faster flow speed which increases the throughput of the device. This could also decrease the field of view or increase the cost of the sensor. Some larger detectors can be partitioned to read out different sections of the chip at separate times to maintain a high frame rate and field of view. The two classes of detectors are complementary metal-oxide semiconductors (CMOS) or charge-coupled devices (CCD). CCD sensors typically have larger pixel counts and lower noise when compared to CMOS sensors; however, the size of the individual pixels are larger than $4\text{--}5\mu\text{m}$, which significantly limits their resolution when implemented in a lensless imaging device [2].

In order to create a lensless imager, the infrared (IR) filter commonly found atop the sensor must be removed in order to directly access the sensor, either by dissolving the adhesive adhering the two together or manually lifting the window away from the sensor. In order to achieve the best resolution in shadow imaging, the sample must be placed as close to the sensor as possible. Any distance between the sample and the detector results in a great reduction of resolution, regardless of the size of the cells. For instance, if a sample fixed onto a coverslip of thickness $170\mu\text{m}$ is

placed on the sensor, the diffraction pattern arising from it is too great to clearly view any defining characteristics.

The detector chosen for our platform was a Sony IMX219PQ image sensor incorporated into a Raspberry Pi v2 camera and controlled by the Raspberry Pi 3. This is a CMOS image sensor with a $1.12\mu\text{m}$ pixel size, an active area of 3280×2464 pixels and a field of view of $\sim 2.7\text{mm}\times 3.6\text{mm}$. It can capture a single image at its full field of view. At 30 frames per second (fps), it captures video at a resolution of 1920×1080 using a partial field of view, without binning. Framerates from 40-90fps involve a partial field of view and 2×2 pixel binning. The Pi v2 camera is backside illuminated, meaning the photodiode is embedded in the top layer of the sensor allowing samples to directly contact the pixel surface with minimum distance[3]. This detector was chosen for its small pixel size and ease of use, allowing the capture of high resolution images.

In order to access the image sensor, the lens and IR filter are gently removed from it (Fig. 4.3a,b). The Raspberry Pi v2 camera can come with or without an IR filter. In the case of the Raspberry Pi v2 No IR camera, there is a piece of glass in place of the IR filter. In either case, this window (IR or not), must be removed. The lens and IR filter are encased in a plastic holder and adhered to the sensor. The sensor is connected to the camera board via a sunny connector. First, the sensor is detached from the camera board and placed on a 70°C hot plate for 10 minutes in order to melt the glue. The plastic casing is then firmly pulled off of the sensor with a pair of needle-nose pliers. Once the sensor is freed it must be handled with extreme caution to avoid soiling the sensor or breaking the gold bond wires.

In order to protect the gold bond wires around the CMOS (Fig. 4.3c), polydimethyl-siloxane (PDMS) at a 1:10 ratio of polymer to initiator was placed onto the sensor and spin coated for 30 seconds at 3000rpm. This was left to cure for 2 hours at 65°C in an oven. If the gold bond wires are not coated, the sensor is easily damaged. If the fluid sample comes into contact with the gold bond wires, while the sensor is on, the sensor will short and cannot be reused. If the channel is placed on an uncoated sensor and pressure is applied, the gold bond wires are at risk of detaching and the sensor will break. In order to avoid this, the PDMS coats the bond wires and acts as a cushion to prevent detaching. The sensor must continue to be handled with caution as the PDMS layer is easy to damage which causes large artifacts in the image. Although this is able to protect the CMOS sensor, it increases the distance between the sample and the sensor and causes a significant decrease in resolution. A longer spin time and faster speed thins the PDMS layer, however not enough testing has been done to determine the optimal thickness of PDMS on the sensor. For the final results, PDMS was not spin coated on the sensor.

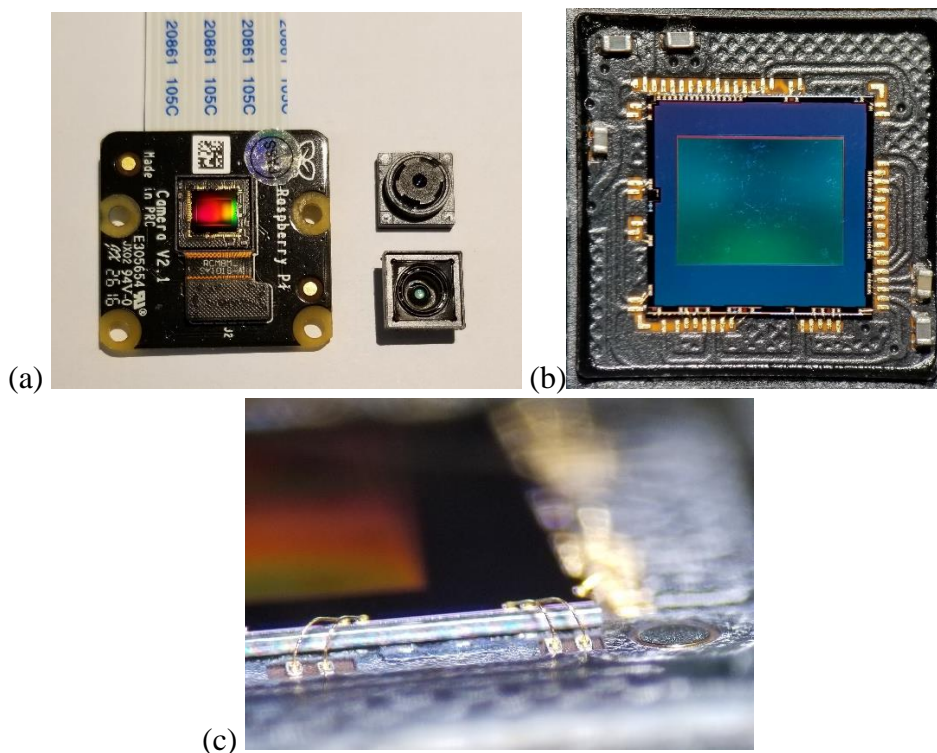


Figure 4.3: (a) Sony IMX219PQ image sensor with the plastic casing holding the lens and IR window removed. The casing is shown with the lens (top) and the IR filter (bottom, flipped) (b) Image sensor without lens and IR filter casing. (c) Gold bond wires are visible around the chip.

4.1.3 Plastic Thin Film for Static Images

Static images of beads and Baker's yeast were taken without a microfluidic device. As the distance between the sample and the sensor is critical to the resolution of the device, a thin plastic layer (plastic wrap of $\sim 12\mu\text{m}$) was used as a layer of protectant for the CMOS sensor. Plastic wrap is charged when dispensed from the roll which may shock the image sensor and cause it to short circuit. To prevent this from happening, the plastic wrap was washed under water with soap and dried thoroughly and gently with a paper towel before being placed on the sensor. A solution of beads (Polybead® Carboxylate Microspheres, Polysciences, Inc.) can then be diluted and dropped onto the surface and allowed to dry. In the case of cells, which were not allowed to dry on the thin film, two plastic layers were used to seal the cells between them. This method proved to be a poor sample holder in the long term as the plastic film often broke and the sample leaked onto the detector, breaking it.

4.1.4 Microfluidic Device for Optofluidic Imaging

The microfluidic channel in an optofluidic setup is highly sample dependent. Urine samples often contain particulates that range from $1\mu\text{m}$ to $50\mu\text{m}$, so in the simplest channel the height must accommodate the largest particle. In general, they are fabricated by creating a mold through photolithography and filling this mold with PDMS. Photolithography is a very versatile technique that allows for the creation of microfluidic channels of different heights, lengths, and widths. The length of the channel should cover the length of the detector for a maximum field of view, and the width of the channel is dependent on the active pixel area on the sensor. If rapid

single cell screening is the goal of the device, the active pixels on the sensor can be adjusted to suit the width of the channel, which would be slightly larger than the width of the cell. This way the detector can rapidly read out the images taken of the single stream of cells in the channel. If there is a mosaic of cells, such as in urine, a wider channel can be fabricated to allow passage of all shapes and sizes of specimen.

Molds were fabricated in the CEDT cleanroom. A mask was ordered from CAD/Art Services (outputcity.com) with five potential channel designs (Fig. 4.4). Silicon substrates with a three inch diameter were cleaned first in acetone, then methanol, then rinsed with deionized water for approximately two minutes each. They were dried with nitrogen and placed on a hotplate set to 150°C for two minutes. Once cooled, the silicon substrates were placed in a plasma cleaner for one minute. Approximately three milliliters of SU-8 2025 was poured directly onto the center of the silicon with as few bubbles formed as possible. The silicon was then spun at 500rpm for 10 seconds, and subsequently 4000rpm, 1750rpm and 1000rpm for 30 seconds to achieve thicknesses of $\sim 20\mu\text{m}$, $\sim 50\mu\text{m}$, and $\sim 80\mu\text{m}$, respectively. The rest of the procedure for SU-8 2025 permanent epoxy negative photoresist on MicroChem was followed for each disk from the SU-8 2025-2075 Data Sheet [4].

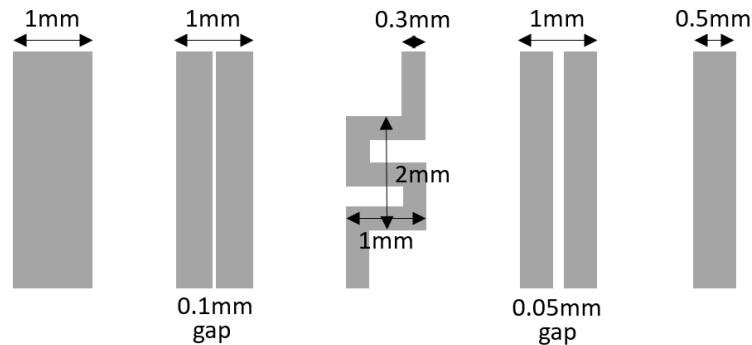


Figure 4.4: The design and dimensions of the five channels. The lengths of the channels are all 5cm. Every channel was made with three different heights, $20\mu\text{m}$, $50\mu\text{m}$, and $80\mu\text{m}$. A. Straight channel, 1mm in width. B. Two parallel channels $400\mu\text{m}$ wide with a $100\mu\text{m}$ divider between them for added support. C. $300\mu\text{m}$ wide “S” shaped channel. The full S spans the active area of the channel. D. Two parallel channels $475\mu\text{m}$ wide with a $50\mu\text{m}$ divider between them for added support. E. Straight channel, $500\mu\text{m}$ in width.

4.1.5 PDMS Channel Fabrication and Optimization

Once the silicon mold was fabricated it was placed into a petri dish and used to cast the polydimethyl-siloxane (PDMS) channels. 15g of polymer and 2g of crosslinker (SLYGARD™ 184 Silicone Elastomer Kit) were mixed well in a plastic beaker and placed in a vacuum chamber until all the bubbles escaped. This ratio of initiator to polymer was chosen to make the channels more resistant to a change in pressure once placed in the final encapsulated device. The PDMS was then poured into the mold and was left to cure in a 70°C oven overnight. Once cured, the PDMS film is peeled from the mold and cut into the five channels in a new petri dish.

Maintaining a clean environment is crucial to having an optically clear channel with no dust particles adhering to it. Inlet and outlet holes were punched out at this stage.

Typically, once fabricated, the channel is bound directly to the detector by air plasma bonding to ensure a minimum distance between the sample and sensor [5]. Although a good technique, with our choice of camera this would mean that the inlet and outlet holes for the channel are placed on top of the active pixel area. These pixels would then be wasted in imaging the inlet and outlet holes, and only a very small area would be used in capturing the steady flow of particles. Instead, we opted to plasma bond the PDMS channel to a thin-film and clamp it to the sensor. In this case the channel is longer and the inlet and outlet holes are not on top of the active pixels. The active pixels only capture the steady flow of particles in the channel. This also allows us to replace the channel without replacing the detector.

Next, to create the thin-film PDMS layer, a 1:10 ratio of initiator to polymer was mixed well in a plastic beaker and placed in a vacuum chamber until all the bubbles escaped. The PDMS was then poured onto a rectangular glass plate covered in Teflon. The glass plate was then transferred to a spin coater (SCS 6800 Spin Coater, Specialty Coating Systems) and spun for 30 seconds at 3000rpm. This corresponds to a thickness of approximately $25\mu\text{m}$, as determined by an optical microscope. A spin time of 30 seconds at 3500rpm also passes the burst test and is preferred for a shorter sample-sensor distance. It was then transferred to a hot plate and left to set for 30 minutes at 90°C . Once cured, the thin-film PDMS layer, still on the glass plate, and the channels were transferred to a plasma cleaner (Basic Plasma Cleaner PDC-32G, Harrick Plasma) for bonding. The PDMS layer was placed face-up in the plasma cleaner, and the channel was placed inside with the channel facing upwards. After 1 minute and 15 seconds in the plasma cleaner, the microfluidic channel was flipped onto the thin-film PDMS layer. The thin-film PDMS on the Teflon was gently cut with a scalpel and the channels were peeled off the Teflon with the thin-film adhered to them. Tape was added underneath the inlet and outlet holes to prevent breakage of the thin-film PDMS once tubing was inserted.

Normally when constructing microfluidic channels, an aspect ratio of 1:10 is crucial for the stability of the channel. The dimensions of the channels were chosen to match the dimensions and active area of the detector for a frame rate of 25fps. This allows us to see the movement of the particles in the channel. At 25fps, the detector has an active pixel area of 2.60mm^2 . The ideal channel would cover the entire active pixel area. This led us to fabricate channels with a width of 1mm, and a length longer than that of the sensor. It also has a height of $\sim 20\text{-}30\mu\text{m}$ to allow large cells and particles to pass through. This channel does not have an aspect ratio of 1:10 and as a result it caves in and the top of the channel sticks to the thin film PDMS on the bottom. By adding height to the channel to achieve a 1:10 aspect ratio, the sample may diffuse vertically and too far away from the sensor resulting in a low resolution. Three different channel heights and five different shapes were tested (Table 4.1).

Table 4.1: Channel optimization. The 1000 μm wide channel with a height of 80 μm had the best flow and shape.

Channel Height	Channel Type	Result
20μm	1000 μm	Channel collapses
	Narrow divider	Channel collapses
	S shape	Channel collapses
	Wider divider	Channel collapses
	500 μm	Channel collapses
50μm	1000 μm	Channel collapses
	Narrow divider	Occasionally uneven flow through top and bottom
	S shape	Slow flow, no benefit to shape
	Wider divider	Occasionally uneven flow through top and bottom
	500 μm	Slow flow
80μm	1000 μm	Great flow - optimal
	Narrow divider	Occasionally uneven flow through top and bottom
	S shape	Great flow, no benefit to shape
	Wider divider	Occasionally uneven flow through top and bottom
	500 μm	Great flow

The channel that was chosen for the final assembly of the device was the channel with an 80 μm height and a width of 1mm. This channel allowed for unperturbed flow and covered the greatest active pixel area. The channels with a 20 μm height all collapsed and the top of the channel adhered to the thin-film PDMS, blocking all flow. The channels with a 50 μm height required a great amount of pressure to flow fluids through and did not result in a higher resolution in comparison to the 80 μm channels.

4.1.6 Assembly

Multiple prototypes were made when determining the best method of assembly for the device. In the first prototype, the channel was simply placed on top of the sensor, however this was not stable and the flexibility of the PDMS resulted in an imperfect seal. This imperfect match between the sensor and channel results in a very poor image in which the thin-film PDMS layer underneath the channel is the main focus in the image. In order for the film to be truly transparent, it must be in contact with the sensor. Krazy glue was used in an attempt to adhere the channel to the sensor, however the glue did not dry. A resin was then applied, however the channel only temporarily adhered to the sensor and it caused the thin-film PDMS to wrinkle. The last and final prototype was assembled with C-clamps. This allows the sensor to be reused with multiple channels.

To assemble the device, the camera was placed in a holder molded from PDMS, and the channel was placed on top of the sensor. This mold supports the channel underneath the inlet and outlet holes enabling the sample to flow through more readily. PDMS is an elastic material and if there is no support underneath the inlet hole, the force of the fluid flowing into the channel causes the thin film below the channel to create a bubble. This bubble can then burst, breaking the channel and the sensor. To prevent this, a piece of tape is placed below the microfluidic channel inlet and outlets. A glass slide is then placed on top of the channel and the assembly is clamped by a C clamp on either side of the glass slide (Fig. 4.5). Specimens were sent through the microfluidic

channel at varying speeds through Tygon S3™ E-3603 Flexible Tubings (Fisher Scientific) (inner diameter 1/16 in., outer diameter 1/8 in.) attached to the inlet and outlet hole. A syringe pump (New Era Pump Systems, Inc., NE-1002X) was used in attempt to keep the flow through the microfluidic channel constant, however it was unable to do so. Low flow rates, below 50ul/min did not push fluid through the channel, and higher flow rates, greater than 50ul/min, pushed the sample through too quickly. As a result, the samples were pushed through the syringe manually.



Figure 4.5: Shadow imaging platform.

4.2 Device Characterization

Characterization of the device began by flowing samples of known size through the microfluidic channel. These included 1 μ m and 10 μ m polystyrene beads. The platform was further characterized with Baker's instant yeast *Saccharomyces cerevisiae*, blood, and *E.coli*. At 25 fps the sensor has a full field of view of 1920 \times 1080 pixels at 1.12 μ m per pixel, translating to 2.60mm². The flow channel, which is 1mm in diameter, covers an area of \sim 2.15mm². At its height of 80 μ m, it is able to hold 0.172 μ l over the field of view (Fig. 4.6).

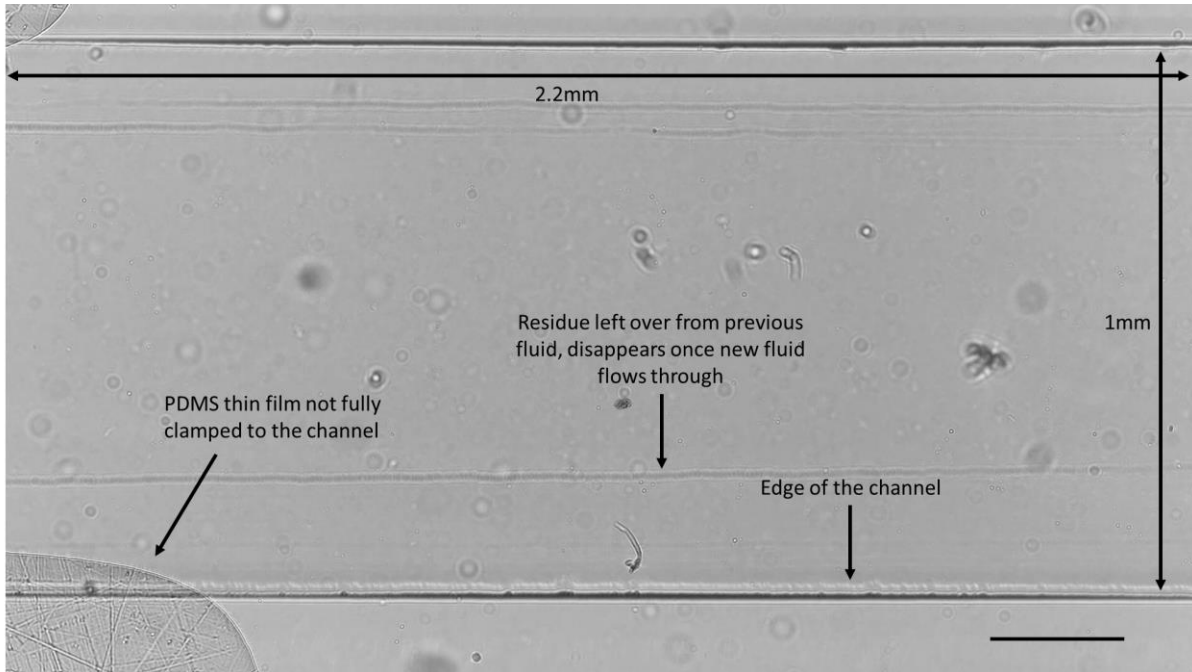


Figure 4.6: Empty channel. The channel is not completely clear as PDMS itself contains particulates. It is also sticky and tends to attract dust and debris. There is a significant difference between the optical clarity when the PDMS thin film at the bottom of the channel is resting flush against the surface verses when it is not properly clamped, as can be seen on the left side of the image. Scale bar 250 μm .

4.2.1 10 μm Beads

The first sample that was used to characterize the platform was 10 μm polystyrene beads. On a plastic thin film of $\sim 12\mu\text{m}$, in which the fluid around the bead was allowed to evaporate and the bead is adhered to the plastic directly on the sensor, the size of the bead is 12 pixels which translated to $\sim 13.4\mu\text{m}$. This indicated a slight magnification of the image onto the sensor (Fig. 4.7).

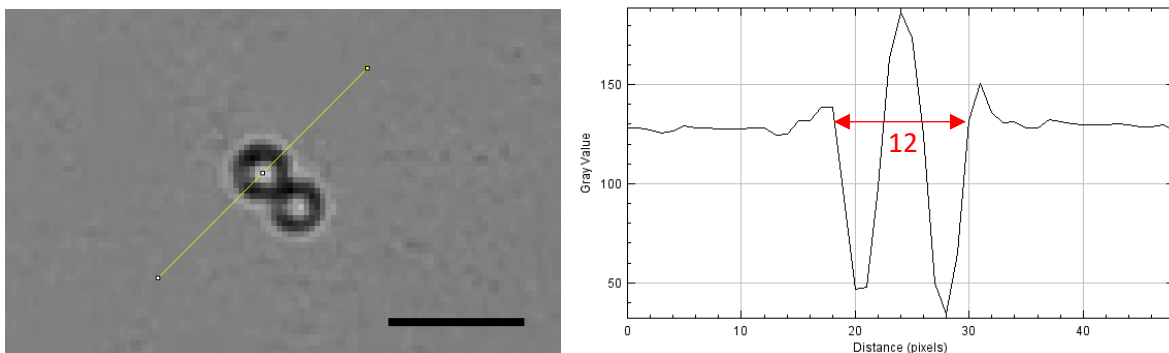


Figure 4.7: (Left) 10 μm polystyrene microbeads on a thin film of $\sim 12\mu\text{m}$. Scale 25 μm (Right) The beads appear to have a size of around $\sim 13.4\mu\text{m}$.

Interestingly, the same bead, prior to drying and adhering to the plastic thin film, has a much brighter center despite measuring at the same size. This may be due to a refractive index change after evaporation of the water (Fig. 4.8).

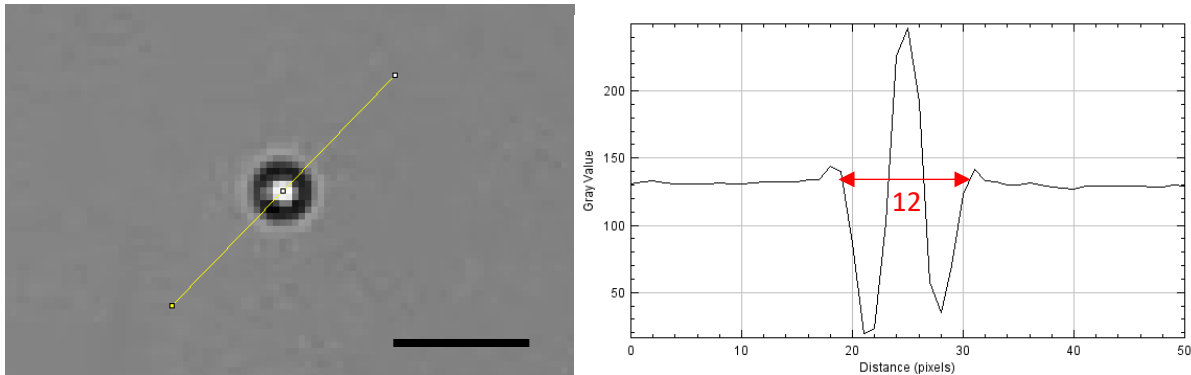


Figure 4.8: $10\mu\text{m}$ polystyrene beads in a water droplet on a plastic thin film. The size of the bead remains the same but the center of the bead is much brighter. Scale $25\mu\text{m}$

When placed in the channel, the size of the bead is 15 pixels which translates to $\sim 16.8\mu\text{m}$ (Fig. 4.9). This expected increase is due to the greater distance between the sample and the sensor. The sensor in this instance is also coated with a thin film of PDMS, and the sensor-sample distance is estimated to be $>40\mu\text{m}$. The size of the bead does not change, regardless of where the bead is in the channel, indicating a stable flow that holds the bead at the same height above the sensor.

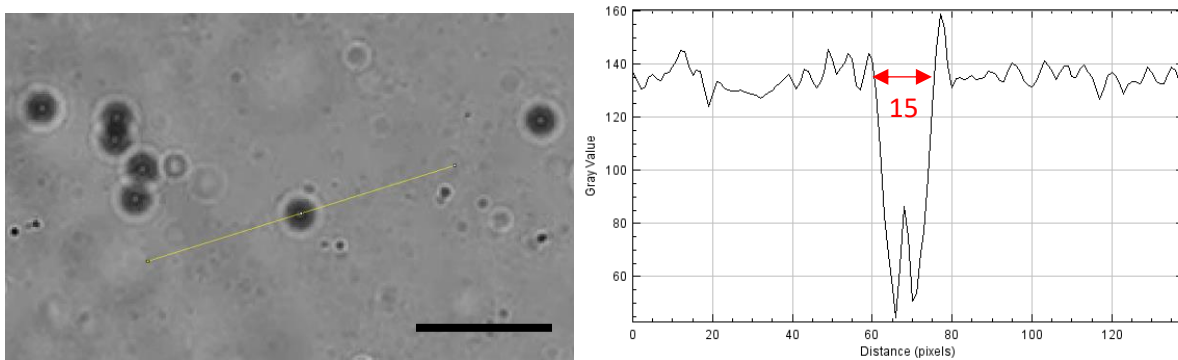


Figure 4.9: (Left) $10\mu\text{m}$ beads in a microfluidic channel with a height of $80\mu\text{m}$. Scale $50\mu\text{m}$ (Right) The size of the beads now appears to be $\sim 16.8\mu\text{m}$.

4.2.2 $1\mu\text{m}$ Beads

Next, smaller $1\mu\text{m}$ beads were tested on the lensless platform atop a thin film and the image was compared to that from a Leica inverted brightfield microscope under $400\times$ magnification (Fig. 4.10). The images from the brightfield microscope and lensless platform bear resemblance to one another, however the resolution of the sensor is not high enough to distinguish between two $1\mu\text{m}$ beads beside one another.

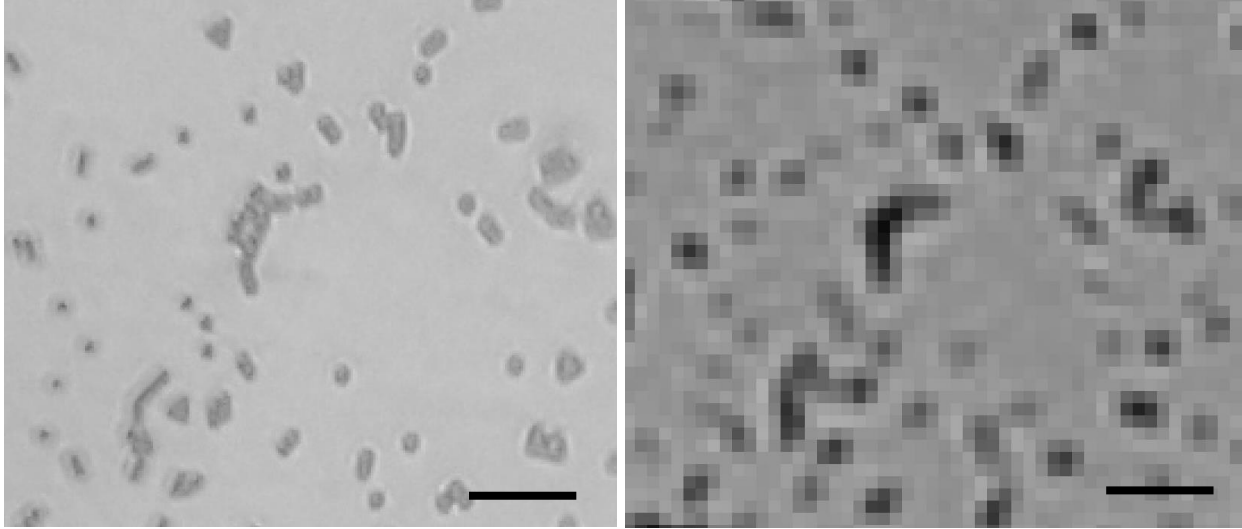


Figure 4.10: (Left) $1\mu\text{m}$ beads on a brightfield microscope with a $40\times$ objective. Scale $10\mu\text{m}$ (Right) $1\mu\text{m}$ beads on the lensless platform. There are clear similarities between the images, however it is difficult to resolve the distances between the beads in the lensless image. Scale $10\mu\text{m}$

The beads were also placed in a microfluidic channel to test how that might change their appearance (Fig. 4.11). The $1\mu\text{m}$ beads in the channel have a much larger appearance due to the diffraction of the light around the bead. Although the bead is faintly visible, it would not be easily identifiable in a channel with other specimen present.

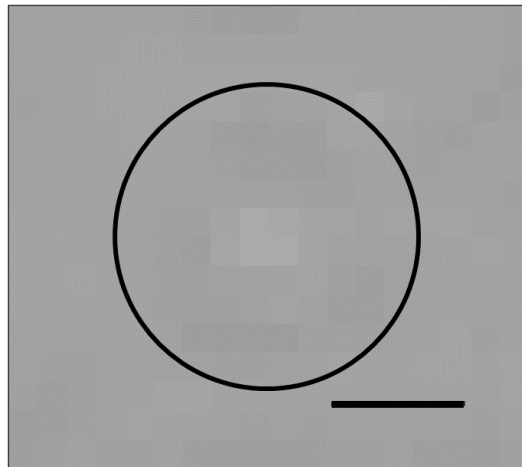
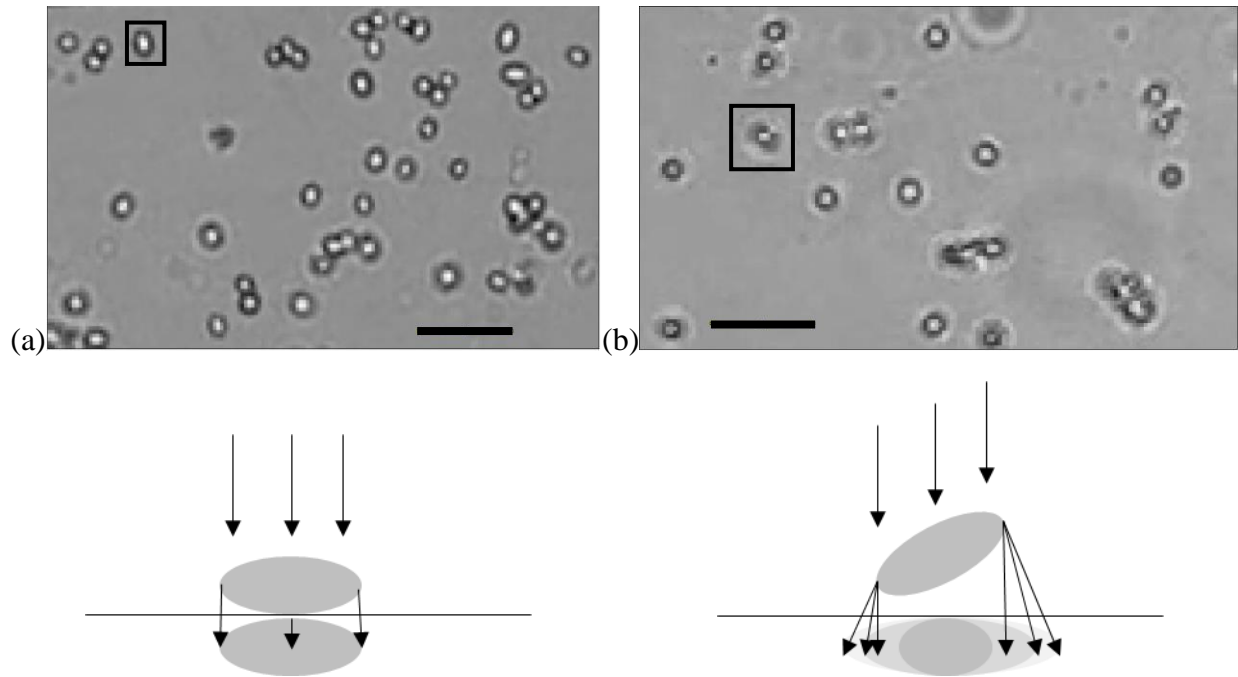


Figure 4.11: $1\mu\text{m}$ bead in a microfluidic channel on the lensless platform. Scale bar $5\mu\text{m}$.

4.2.3 Yeast

Yeast, when placed on a thin plastic film, has a circular to ovoid shape, however this characteristic shape can be lost when placed in the microfluidic channel (Fig. 4.12). On the thin plastic film, the yeast is not suspended in water, but lying flat on the film. This allows for very little potential for diffraction. When flowing through the channel, the potential for diffraction is

increased, and this creates a defined core with undefined “wings”. The yeast in the channel also have a brighter halo around them.



*Figure 4.12: (a) (Top) Baker's instant yeast *Saccharomyces cerevisiae* on a plastic thin film. Scale bar 30 μ m (Bottom) The diffraction of light through the yeast and onto the sensor is minimal as there is not a great enough distance between the yeast and the detector to allow the light rays to disperse (b) Baker's instant yeast *Saccharomyces cerevisiae* in a microfluidic channel of height 80 μ m. Scale bar 30 μ m. (Bottom) The diffraction of light through the yeast and onto the sensor is larger as there is a larger distance between the yeast and the detector allowing the light rays to disperse*

4.2.4 Blood Cells

Next, whole blood was diluted in 1 \times PBS pH 7 and flowed through the channel (Fig. 4.13; **Supplementary Figure 1**). The red blood cells (RBC's) are easily distinguishable due to their unique morphology. They have a divot in the center of the cell which appears as a shadow. This biconcave shape also causes the cells to flip repeatedly in the channel, as opposed to the rolling observed from other particles. The blood cells readily adhere to the PDMS indicating a hydrophobic coating should be applied prior to sample flow. The cells appear to be around 13-15 μ m in the channel, whereas they are supposed to measure in at around 6-8 μ m. It is possible that cells have swollen due to osmotic pressure once they were diluted in PBS.

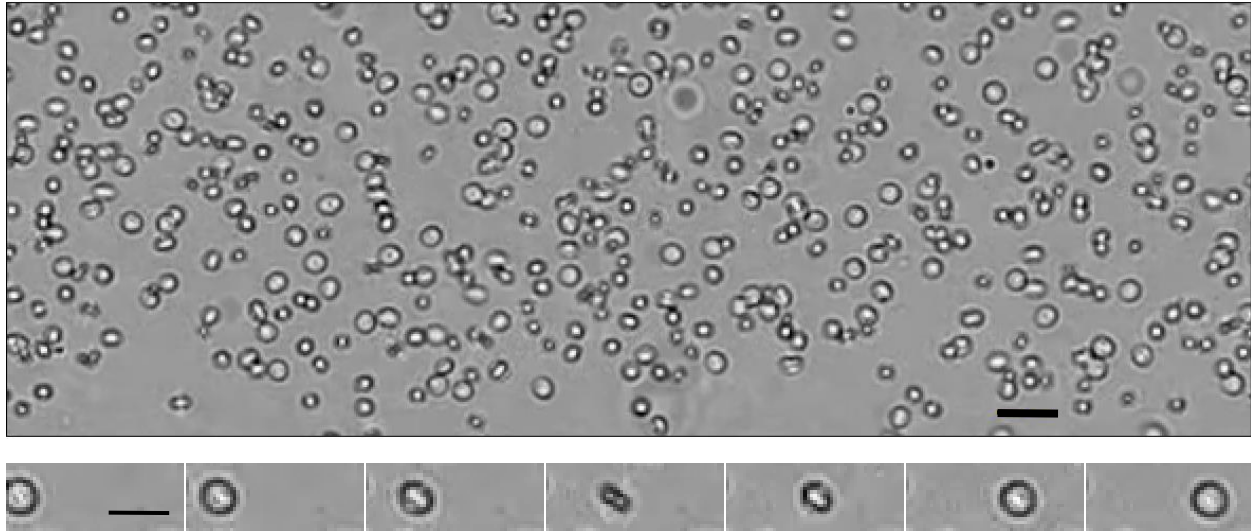


Figure 4.13: (Top) Diluted blood flowing through the channel. The biconcave shape is an easy morphological feature to spot. The smaller, brighter particles in the image without the divot in the center are predicted to be damaged red blood cells. Scale bar $30\mu\text{m}$. (Bottom) A red blood cell flipping as it moves along the channel. Scale $15\mu\text{m}$

4.2.5 *E.coli*

The final sample that was placed on the channel for characterization purposes was *E.coli*. Bacteria are very small, $\sim 1\mu\text{m}$, and highly transparent. Usually, the *E.coli* is stained prior to imaging on a brightfield microscope, or they are placed on a phase contrast microscope without staining. This makes imaging on a lensless microscope challenging. The sample was placed between two pieces of a plastic thin film first (Fig. 4.14 (a)). They are very difficult to differentiate from background noise in a static image, but when in a video they are more noticeable. When placed in a microfluidic channel at a high concentration (10^9 cfu/ml) the bacteria resembles noise and it is difficult to differentiate individual cells (Fig. 4.14 (b)).

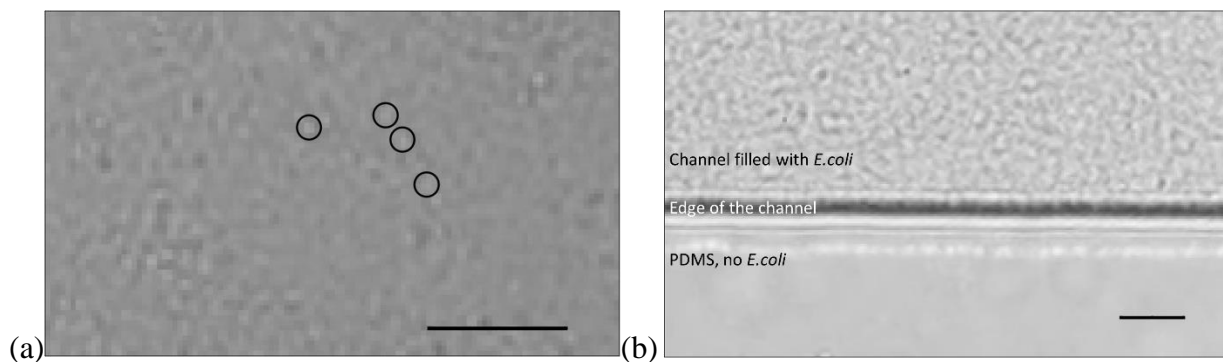


Figure 4.14: *E.coli* in between a plastic thin film (b) *E.coli* in an $80\mu\text{m}$ channel height. Overnight culture at 10^9 cfu/ml. Scale bar $30\mu\text{m}$

4.3 Discussion and Conclusion

This chapter covered the design, fabrication, and characterization of the lensless optofluidic device developed for urine analysis, however, this prototype can be further optimized. The light

source that is being used is a 1W LED desk lamp. In order to reduce the size of the device and compact it into a point-of-care device, an LED with a variable power source can be used. It can be coupled with a diffuser and placed within 5cm above the sample to allow for uniform illumination.

The detector that is being used, a Raspberry Pi v2 camera, is beneficial for multiple reasons. There is no need to set up the camera with external drivers, and there are no compatibility issues. The detector is being controlled by a Raspberry Pi, an easily programmable minicomputer. These two parts are also very low cost, if purchased in bulk they can be less than \$50 together. The image sensor also has a very small pixel size at $1.12\mu\text{m}$ allowing for a fairly high resolution for a shadow imaging device, and the IR window is easily removable providing full access to the detector. A step that can be taken to improve the usability of the sensor is to coat the gold bond wires with an agent that allows for conductivity but prevents their breakage. PDMS was used to coat the bond wires, however the sample-sensor distance was too large and the resolution of the videos suffered. A thinner coat of PDMS can be used in this case.

The detector also has a 2.60mm^2 field of view, however only $\sim 2.15\text{mm}^2$ is being used to detect sample flow due to the width of the microfluidic channel. This can be extended slightly to take advantage of the entire active pixel array. At its height of $80\mu\text{m}$, it is able to hold $0.172\mu\text{l}$ over the field of view. This height allows all of the components of urine and blood to pass through without issue. At smaller heights there was difficulty in achieving rapid flow. It was also noted that after a few seconds of continuous flow, a large amount of debris began to accumulate on the surface of the channel. This is an indication that coating the inner surface of the channel is crucial to keeping it clean. Various coatings have been previously used to prevent the fouling of biological organisms on PDMS [6].

The assembly of the device is unique to lensless imaging devices. To our knowledge, there has not been a lensless imaging device that utilized pressure to achieve a small sample-sensor distance. The clamps allow the adjustment of the height of the microfluidic channel over the sensor. The sensor can also be reused as the channel is easily replaced. Normally, the channels are plasma bonded directly onto the sensor which decreases the lifespan of the entire device due to the gradual degradation of the channel and its inability to be removed from the sensor. In order to improve the assembly of the device, it must be made to be more user friendly. To accomplish this, an enclosure can be 3D printed to hold the platform. The two clamps can also be replaced by one clamp with alignment markings to help guide the placement of the microfluidic channels.

The images of known samples attained from the setup are used to characterize the platform. The $10\mu\text{m}$ beads and yeast that were placed on the plastic thin film, (Fig 4.8a and 4.12a), seemed to have developed a brighter center as the liquid medium evaporated. This effect may be occurring because of the formation of a liquid micro-lens on top of each particle which focuses the light onto the sensor. The thin wetting film, which is created as the liquid medium evaporates, acts as a plano-convex micro-lens. This was used as a technique to amplify the signal of *E.coli* in Allier *et al.* [7].

In viewing the 10 μm beads, we are able to determine that there is magnification of the sample. At a distance of $\sim 12\mu\text{m}$ away from the sensor, the beads appear to have a size of 13.4 μm . In the microfluidic channel of height 80 μm , they appear even larger at 16.8 μm . This difference in width appears to be even more significant with the 1 μm bead. Once placed in an 80 μm tall channel, the 1 μm bead is barely visible, and seems to spread out over a diameter of almost 9 μm . This confirms that there is a very sensitive requirement for the sample-sensor distance. Smaller particles seem to be amplified in size more so than large particles, this also applied to the RBCs. This could be because the 1 μm beads found in the channel are actually aggregates, and we cannot resolve any distance between them, and the RBCs have swollen due to osmotic pressure. The particles do not change size as they flow through the channel, indicating that they hold a fairly stable position above the sensor.

The videos of RBCs and yeast in the channel confirmed that there are defining features for these components that can be exploited to create an algorithm for automatic detection. These arise due to their morphology and the resulting shadow image.

The challenge of imaging bacteria is congruent with its size and transparency. Bacteria are $\sim 1\mu\text{m}$ and essentially transparent. A very high concentration of bacteria was used to test the device, but a better representation of the detection limit would be a dilution experiment with ground truth analysis. Stains for fixed bacteria, like methylene blue, would not be used in a ground truth experiment. These stains are meant for dead bacteria and are reduced in the presence of live bacteria. Bacteria expressing fluorophores can be used as ground truth. The optofluidic microscope can be placed on an upright fluorescent microscope and the sample of bacteria can be measured by both simultaneously. This way the presence of individual bacteria in the channel can be confirmed.

The next step in the development of the platform is to test positive and negative urine samples and identify their components.

References

- [1] S. A. Lee and C. Yang, “A smartphone-based chip-scale microscope using ambient illumination,” *Lab Chip*, vol. 14, no. 16, pp. 3056–3063, Jul. 2014.
- [2] A. Ozcan and E. McLeod, “Lensless Imaging and Sensing,” *Annu. Rev. Biomed. Eng.*, vol. 18, no. 1, pp. 77–102, Jul. 2016.
- [3] X. Huang *et al.*, “Machine Learning Based Single-Frame Super-Resolution Processing for Lensless Blood Cell Counting,” *Sensors*, vol. 16, no. 11, p. 1836, Nov. 2016.
- [4] “MicroChem SU-8 2000,” *MicroChem Corp.*, 2019. [Online]. Available: <http://www.microchem.com/Prod-SU82000.htm>.
- [5] X. Cui *et al.*, “Lensless high-resolution on-chip optofluidic microscopes for *Caenorhabditis elegans* and cell imaging,” *Proc. Natl. Acad. Sci. U. S. A.*, vol. 105, no. 31, pp. 10670–5, Aug. 2008.
- [6] G. Zheng, S. A. Lee, S. Yang, and C. Yang, “Sub-pixel resolving optofluidic microscope for on-chip cell imaging,” *Lab Chip*, vol. 10, no. 22, p. 3125, Oct. 2010.

- [7] C. P. Allier, G. Hiernard, V. Poher, and J. M. Dinten, “Bacteria detection with thin wetting film lensless imaging,” *Biomed. Opt. Express*, vol. 1, no. 3, p. 762, Oct. 2010.

Chapter 5.

Urine Analysis

Lensless imaging is an applicable and versatile technique in the field of health monitoring and diagnostics. This thesis aims to demonstrate that with appropriate modifications, a point-of-care lensless optofluidic device can be developed to detect small particles in urine and contribute to patient diagnosis. These include red and white blood cells, casts, crystals, and pathogens like *Trichomonas vaginalis* parasites and bacteria. Determining the presence of these particles in urine can contribute to an accurate diagnosis. A full list of particulates can be found in Chapter 2. This chapter illustrates that shadow imaging is an effective technique in visualizing the components of urine and determining identifiable characteristics, which is a critical step in developing an accurate diagnostic tool.

5.1 *Trichomoniasis*

Trichomoniasis is estimated to be the most common non-viral sexually transmitted infection in the world, with 276.4 million cases worldwide in 2008 [1]. It is more commonly present in minorities and areas with lower income and lower education and often goes undiagnosed. The clinical presentation of trichomoniasis is similar to that of urinary tract infections indicating that a universal urine analysis test would be a useful diagnostic tool to differentiate between different conditions with similar symptoms.

It is an infection caused by *Trichomonas vaginalis*, a parasite 10–20 μm in length and 2–14 μm in width. It has commonly been diagnosed through wet mount microscopy, indicating that morphology is a defining factor for identification. Unfortunately sensitivities range from 50-70% depending on the reader [2]. Continuous sample flow over the field of view and automated detection based on the morphological features of the parasite can be implemented in an effort to increase the sensitivity.

Normally, it is critical to minimize the distance between the sample and the sensor for projection imaging in order to maximize the resolution, however, we illustrate that when screening for *Trichomonas vaginalis*, a greater distance is more advantageous. Here we present a lensless optofluidic imaging technique for label-free detection of motile parasites, by using the parasites natural ability to focus light as a contrast mechanism.

5.1.1 *Characteristics*

A drop of *Trichomonas vaginalis* culture was first placed between two thin plastic thin-films, ~12 μm in thickness, and placed directly on the sensor. This allowed for the minimization of the

distance between the sample and the detector, and confined the parasites to a shallow chamber, preventing them from drifting upwards and away from the sensor. *Trichomonas vaginalis* was identified by its elongated morphology and its characteristic locomotion (Fig 5.1(a)). This parasite tends to spin in circles and swim from one area to the next. It can also “stand” vertically, perpendicular to the sensor (Fig 5.1(b)). In this orientation, the center of the parasites have an increase in intensity, uncharacteristic of brightfield microscopy where the center of the cell is normally darker than its surroundings due to the attenuation of light. In order to test this theory, 22 parasites, oriented in equal parts vertical and horizontal, were analyzed (Fig 5.1(c)). Intensity histograms were used to determine the pixel intensities across the length of the parasites. A t-test was conducted between horizontal and vertically oriented parasites with a result of 11.74, higher than the critical value of 2.04; thus, we reject the null hypothesis and conclude that there is a significant change in intensity between the groups. It is possible that the parasite is able to focus the light onto the detector in this orientation. With this in mind, we were able to further adapt the device.

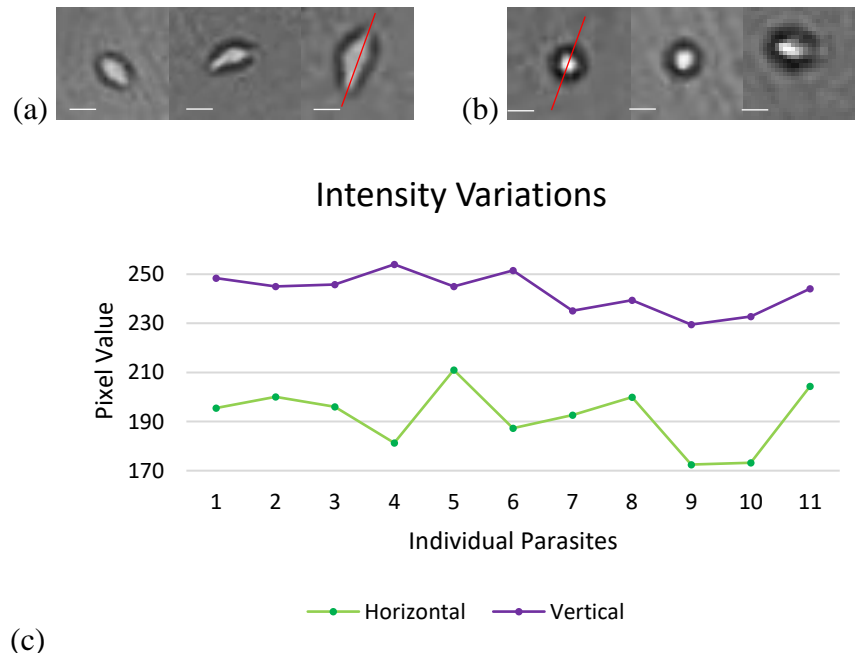


Figure 5.1: (a) Multiple *Trichomonas vaginalis* laid flat, parallel to the sensor. The characteristic morphology is visible in the image and its locomotion is visible in the video. Scale bar: $10\mu\text{m}$ (b) Multiple *Trichomonas vaginalis* “standing” vertically in the channel, perpendicular to the sensor. Through visual analysis alone, there seems to be a change in intensity based on the orientation shift. The red bars in a and b indicate the axis through which the intensity histograms were created. Scale bar: $10\mu\text{m}$ (c) A plot of the variation in intensity of the parasites in the horizontal and vertical orientations. There is a significant change in intensity between the two groups.

In order to create a high-throughput imaging device, we then flowed *Trichomonas vaginalis* through a microfluidic channel. This channel is 80 μm in height, and 1mm in width. Within this channel, the *Trichomonas vaginalis* are further from the sensor and can focus the light in any orientation better than in the previous setup. In a channel that is placed $>50\mu\text{m}$ away from the sensor, the parasites are much brighter than their surroundings, but lose their characteristic oblong morphology (Fig. 5.2(a)). In a channel that is placed $<20\mu\text{m}$ away from the sensor, the parasites retain their oblong morphology and bright center (Fig. 5.2(b)). $<20\mu\text{m}$ is the sample-sensor distance chosen for the analysis of all specimen on the device.

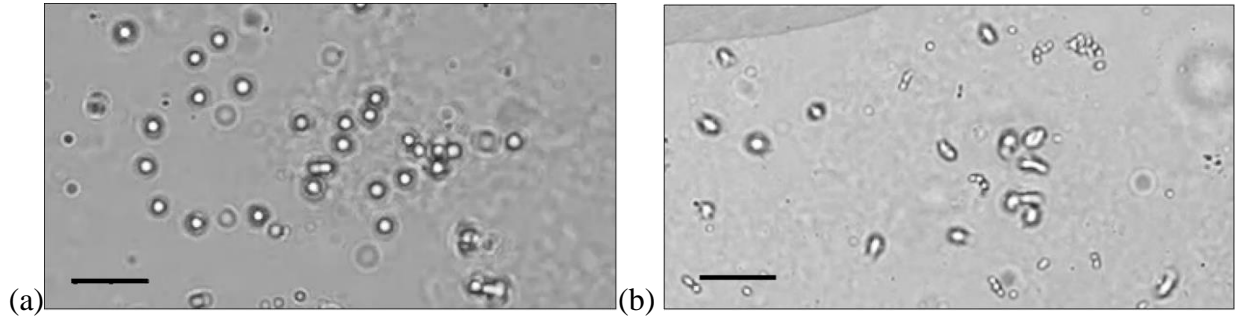


Figure 5.2: (a) *Trichomonas vaginalis* in a channel $>50\mu\text{m}$ from the sensor. The parasites lose the characteristic oblong morphology. Scale $50\mu\text{m}$. (b) *Trichomonas vaginalis* in a channel $<20\mu\text{m}$ from the sensor. The parasites retain their oblong shape for the most part. Scale $50\mu\text{m}$.

5.1.2 Identification

Trichomonas vaginalis is identifiable in the channel by its brightness which is believed to be caused by its ability to focus light onto the sensor, alleviating the need to have a shallow channel, and allowing the use of a sample holder further from the sensor. We are able to isolate the *Trichomonas vaginalis* in the channel as they are brighter than the rest of the cells and debris in the channel.

The 24-bit 1920×1080 pixel .h264 video file is converted to a set of .tiff image files with the command line program FFmpeg, a free software that is used to manipulate audio and video formats. The frames are then imported into ImageJ as a stack and converted to 8-bit grayscale images. The maximum filter is applied to the stack of images. This filter replaces each pixel in the image with the largest pixel value in that pixel's neighborhood. The stack is then binarized and particles smaller than 15 pixels are eliminated. The workflow for the algorithm is found in Fig. 5.3. The final step in the algorithm, particle analysis, is part of future work. Counting algorithms can be implemented after the identification of the parasites. Motion tracking and optical flow algorithms would be able to determine the viability of the parasites as they have a specific locomotion.

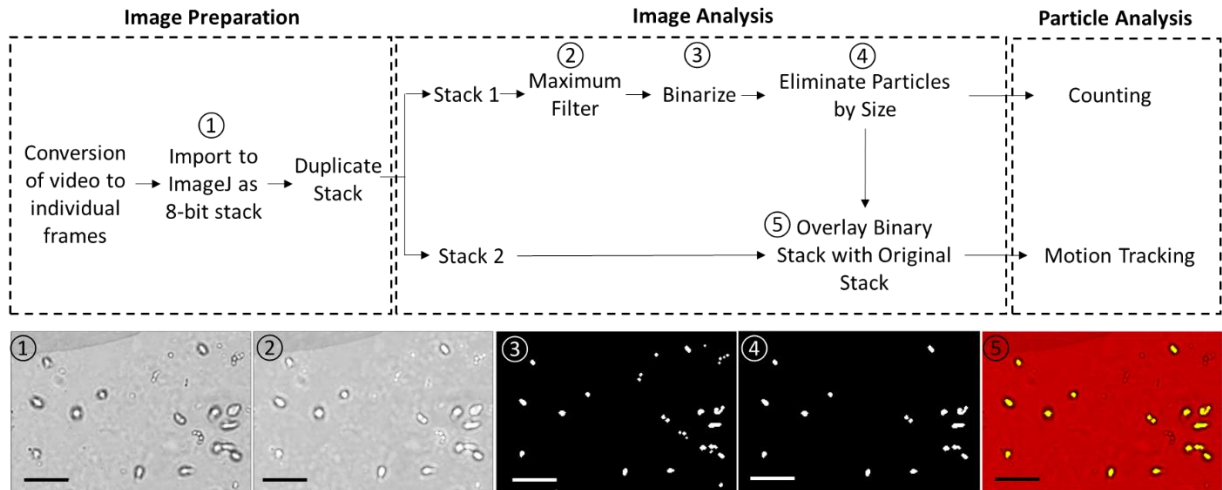


Figure 5.3. Concise workflow of the algorithm for the processing of the lens-free shadow image. Bottom pictures show how the original image is transformed at critical steps.

This method of analysis does not highlight every individual *Trichomonas vaginalis* parasite in every frame, but over the course of several frames, as the parasites move around, the algorithm is able to highlight them (Fig. 5.4; **Supplementary Figures 2 and 3**). This is because as the parasites move around the channel, they take up a larger or smaller area. If they change position such that they occupy a space smaller than 15 pixels, they will not be identified. This pixel area was chosen strategically. If the area was smaller, there are too many false positives, and if the area is enlarged there are false negatives.

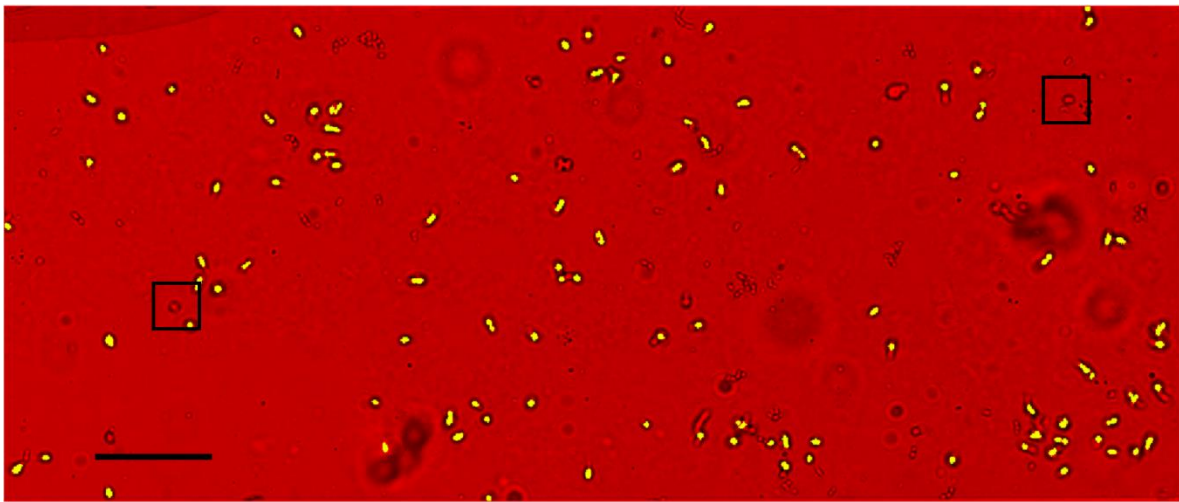


Figure 5.4. One quarter of the full field of view of the microscope. Some parasites are not identified, as can be seen in the black boxes. These are false negatives in this frame, but are later identified in other frames. Scale $100\mu\text{m}$.

The culture of parasites was then diluted with a urine sample that was negative for the presence of bacteria in order to test whether other naturally occurring specimen in urine would be identified with this image processing method (Fig. 5.5(a,b)). We were able to see that there was

no change in the identification of the parasites when diluted in urine. The image processing method was still able to detect the parasites accurately. There was a false negative signal at the bottom left of the channel where the thin-film PDMS lifted off the sensor (Fig 5.5 (b)). This can be avoided by placing more pressure on the sensor with the clamps.

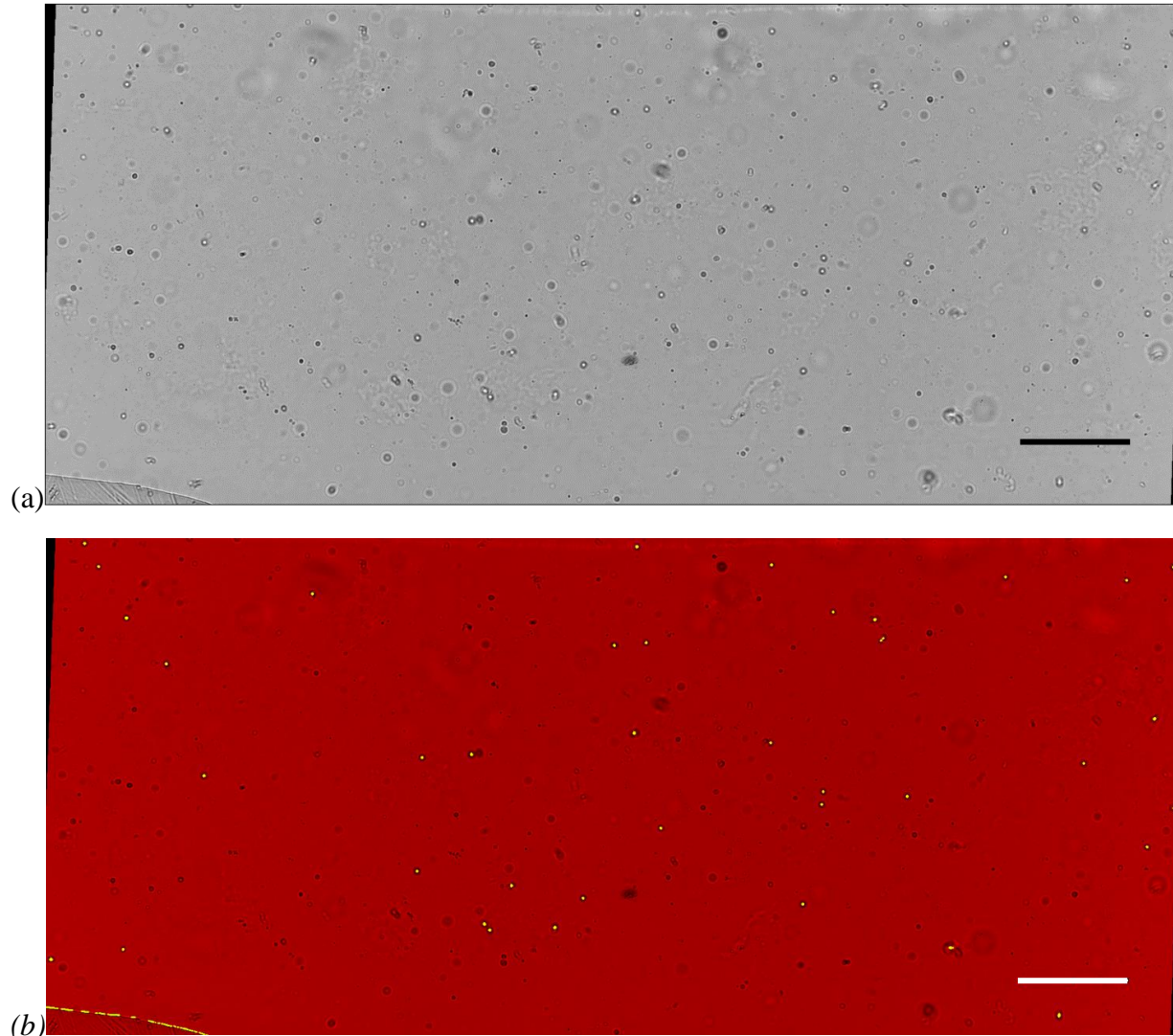


Figure 5.5. (a) Full field of view of Trichomonas vaginalis diluted in a urine sample and flown through the channel. (b) Full field of view of Trichomonas vaginalis being identified in the channel despite being diluted in a urine sample. Scale 200µm

Further investigation into developing a more sensitive detection algorithm did not result in any leads. An attempt was made to average the frames in order to get a time-lapsed imaged of the spinning parasites and use it as a unique identifying feature. This simply resulted in the disappearance of the parasites and retention of the background.

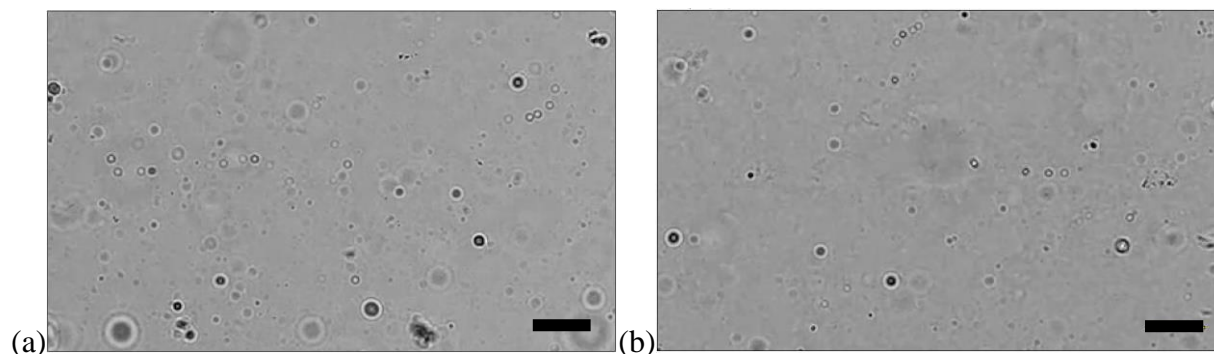
5.2 Urinary Tract Infections

Urinary tract infections are caused by an overgrowth of bacteria in the urinary tract and affect almost 50% of the population at least once in their lifetime, leading to an annual health care cost of approximately \$3.5 billion in the USA. Current detection techniques take up to 48 hours and 60-80% of samples come back negative. As well, antibiotic administration often occurs prior to receiving the test results. Both patients and the health care system would benefit significantly from the immediate feedback of samples, if even just to eliminate the negative samples from further processing.

The current gold standard of bacterial detection in urine is plating them on agar and awaiting growth. This allows for the identification of the type and amount of bacteria present in the sample. The disadvantage of this technique is the 24-48 hour turnaround time. Imaging the bacteria directly from the sample would decrease this turnaround time significantly, however the challenge of imaging bacteria is congruent with its size and transparency. Bacteria are $\sim 1\mu\text{m}$ and transparent. In order to visualize bacteria on a standard brightfield microscope, they are fixed to a glass slide and stained. They can also be visualized on a phase contrast microscope without staining. Both of these techniques involve large and expensive hardware as well as trained pathologists to manually mount, stain, and identify the samples. The ideal optical solution would be able to automatically identify the presence of bacteria with minimal sample preparation and intervention. In the previous chapter we determined that bacterial culture at a high concentration was easily detected in the microfluidic channel. In this section we will determine whether that is also the case for bacteria found in urine samples.

5.2.1 Identification

Similar to the cultured bacteria, bacteria in urine is difficult to identify. Positive and negative urine sample were retrieved from Hamilton General for analysis. The samples were checked for growth after 48 hours on an agar plate. If there was no growth, the samples were identified as negative. If there was growth, the samples were identified as positive and placed into three categories defined by the number of colony forming units counted on the plate: $<10\text{CFU}$, $10\text{-}100\text{CFU}$, and $>100\text{CFU}$. The positive and negative samples were then tested on the optofluidic imaging platform without any sample preparation (Fig. 5.6; **Supplementary Figures 4 and 5**).



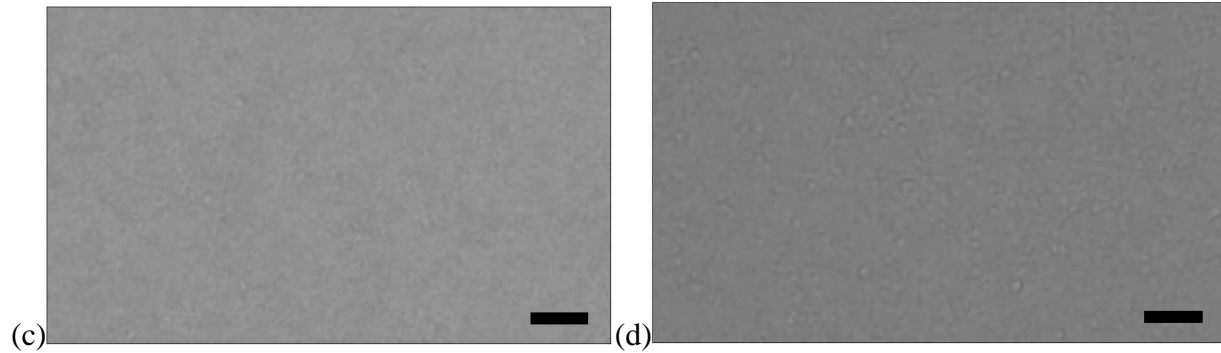


Figure 5.6. (a) Urine sample negative for bacteria. (b) Urine sample positive for bacteria (>100CFU). (c) Negative urine sample with background subtraction. (d) Positive urine sample with background subtraction. Scale 50 μ m

Based on visual inspection of still frames, there is scarcely a difference between the positive and negative samples. The presence of bacteria in the positive urine samples is much less evident than that of the cultured bacteria from the last chapter as well, due to the reduction in bacterial concentration. Despite this, the bacteria in the positive sample becomes more apparent when inspecting the videos. When viewing the videos, the bacteria moving across the channel resembles structured noise. Through the analysis of the still frames, which involved background subtraction and contrast enhancement, the presence of the bacteria were not made to be significantly more evident.

5.3 Crystals, Haline Casts, and Blood Cells

Upon investigation into bacterial detection in urine samples, other components commonly found in urine were detected. Larger particles, which could potentially be damaged red and white blood cells, were commonly found in urine samples positive for the presence of bacteria (Fig 5.6). This is typical as an increase in leukocyte count is normally associated with UTIs. These larger particles were not found in negative urine samples.

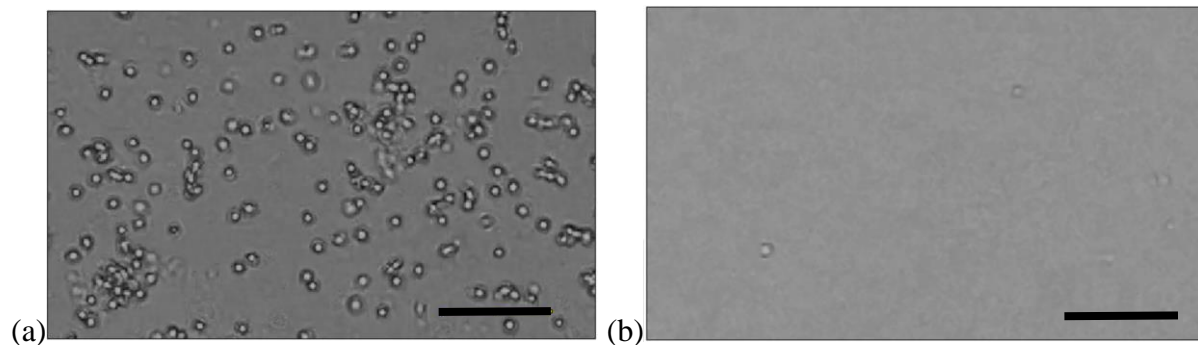


Figure 5.6: (a) Urine sample positive for the presence of bacteria. After background subtraction there is a significant amount of larger particles assumed to be damaged blood cells. (b) Urine sample negative for the presence of bacteria. After background subtraction there are few large particles. Scale 100 μ m.

In our analysis of urine samples, different specimen were found throughout. These include crystals (Fig. 5.7) and haline casts (Fig. 5.8). Casts are used to localize disease to a specific location in the genitourinary tract depending on their composition. Hyaline casts can be associated with pyelonephritis or chronic renal disease. A full list of casts, their morphology, and associated conditions can be found in Simerville *et al.* [2]. The presence of certain crystals, like calcium oxalate crystals and uric acid crystals are normal. Abnormal crystals include cystine crystals which are associated with cystinuria. Crystals form in their own geometric patterns unique to their composition which is a prominent trait to use for automated identification.

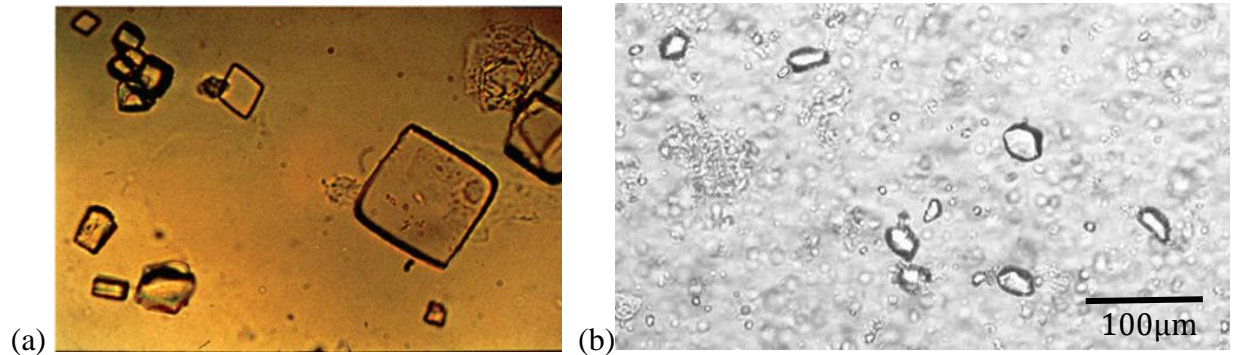


Figure 5.7: Calcium oxalate crystals found in urine under (a) a brightfield microscope 400x [3] and (b) our lensless shadow imaging microscope

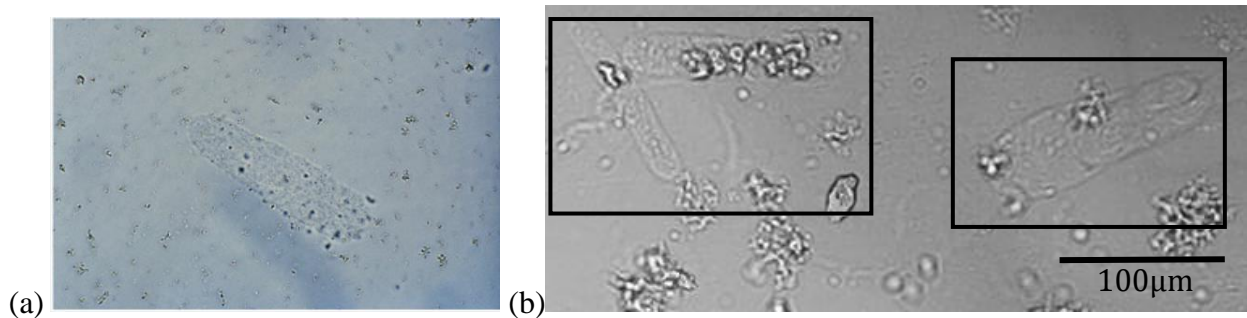


Figure 5.8: Haline cast found in urine under (a) a brightfield microscope 400x [3] and (b) our lensless shadow imaging microscope

5.4 Discussion and Conclusion

Due to the diversity of the specimen that can be found within urine, creating a cost-effective and universal point of care analysis device is quite challenging. In order to identify each specimen accurately, several defining characteristics must be chosen. Certain features have been identified, however, some particulates have features that are easier to define than others.

We have demonstrated that *Trichomonas vaginalis* can be identified based on its oblong morphology and bright center. The drawback to this method is the lack of specificity. Although we have noted that a specific quality of *Trichomonas vaginalis* is that it has a bright center, if there is another particle that enters the frame with similar characteristics, it may also be identified as *Trichomonas vaginalis*. The parasite also rotates in the channel causing it to appear circular at times. This can cause misidentification with damaged blood cells that is often found in

urine positive bacterial growth. In order to make a more specific diagnostic tool, the locomotion of the parasite can be exploited. *Trichomonas vaginalis* tends to rotate in a circular motion, which is unique to them. This would also be a measure of viability. This may be possible after investigation into optical flow algorithms that can analyze the rotation of a subject across multiple frames. As well, preliminary use of an open source tracking algorithm has been used to track the parasite as it moves along the channel (Multitracker, from learnopencv.com). It was able to track the parasite despite the change in orientation. This would allow for continual tracking of the parasites. As *Trichomonas vaginalis* is a fairly large and distinct pathogen, once one is detected in urine, a patient can be diagnosed with trichomoniasis. Increasing the amount of urine being screened on the device is an easy way to increase the limit of detection.

Trichomoniasis can be diagnosed through wet mount microscopy where anywhere between <1 and 16 parasites can be found per high power field of 60x [4]. The field of view of a 60x image can be approximated to be $<3\text{mm}^2$, which is comparable to the field of view of our microscope. It is likely that we would be able to detect very low amounts of *Trichomonas vaginalis* with our platform as there is continuous flow of the samples and the parasite is fairly large and distinguishable.

Optically identifying free-floating bacteria is more challenging. The bacteria are $\sim 1\mu\text{m}$ in size and transparent. In a urine sample that has an abundance of bacteria, there is a visible distortion in the video, likened to structured noise. This structured noise can be analyzed as a whole by training a machine learning algorithm with frames of positive samples and frames of negative samples, then testing the algorithm on new frames. This method may be able to differentiate frames with bacteria from frames without bacteria. Cloud computing using Google Colaboratory would allow us to run the algorithm off the Pi in order to remain cost efficient. This method, however, may not be ideal for a low detection limit. The detection of a single bacteria is a much greater challenge.

The limit of detection of the device in bacterial identification is a critical determining factor for its use in diagnosing UTIs. With a diagnostic definition of 10^3 , 1000 colony forming units of bacteria needs to be detected in one milliliter. This is equivalent to $1\text{CFU}/\mu\text{l}$. The volume of urine in the channel above the active pixel sensors at any given time is $0.17\mu\text{l}$. This means that in nearly 6 full flowthroughs, one bacterium must be detected. With all the debris associated with urine, this might be impossible without determining a unique identifying feature of single bacterium. The bacteria can be obscured by other debris in the channel, meaning more of the sample may be needed to get an accurate estimation of the concentration. At $10^4\text{CFU}/\text{ml}$, or $10\text{CFU}/\mu\text{l}$, there would be around two bacteria per field of view. This is still a much lower detection limit than what is currently possible with our device. More evaluation would have to be done to be able to identify a unique signal for individual bacterium in order to reach this detection limit. There are several steps that can be taken for this. More advanced image processing techniques can be used to enhance the resolution of the image, such as multiframe pixel super resolution algorithms. Alternatives to this include staining the urine with a bacteria-specific dye, adding a bacterial concentration step to the microfluidic device, or exploring holography to attain a phase image of the bacteria which may provide more information than an intensity image.

In summary, *Trichomonas vaginalis* parasites can be defined by their morphology and their locomotion. Bacteria can not be identified individually but can be identified when present in large amounts due to the structured noise that appears in the channel. Crystals and casts are very large and easily identifiable based on their morphology. These characteristics can then be used to train an algorithm to automatically identify the specimen. The next step in the development of an accurate diagnosis tool is to be able to use the identifiable characteristics of each component to rapidly and accurately analyze each particle.

References

- [1] P. Kissinger, “Trichomonas vaginalis: a review of epidemiologic, clinical and treatment issues,” *BMC Infect. Dis.*, vol. 15, no. 1, p. 307, Dec. 2015.
- [2] M. A. Kingston, D. Bansal, and E. M. Carlin, “‘Shelf life’ of Trichomonas vaginalis;,” *Int. J. STD AIDS*, vol. 14, no. 1, pp. 28–29, Jan. 2003.
- [3] J. A. Simerville, W. C. Maxted, and J. J. Pahira, “Urinalysis: a comprehensive review.,” *Am. Fam. Physician*, vol. 71, no. 6, pp. 1153–62, Mar. 2005.
- [4] E. E. Doxtader and T. M. Elsheikh, “Diagnosis of trichomoniasis in men by urine cytology,” *Cancer Cytopathol.*, vol. 125, no. 1, pp. 55–59, Jan. 2017.

Chapter 6.

Summary and Discussion

6.1 Summary

Clinical urine tests are valuable diagnostic tools for short and long-term patient care. They aid in the diagnosis of various urologic and renal conditions such as in urinary tract infections and sexually transmitted infections [1]. Urinary tract infections affect almost 50% of the population at least once in their lifetime [2]. Quick and accurate diagnosis is critical to the cost-effective management of UTIs, however, current detection techniques take over 48 hours and up to 80% of samples are negative [3]. Trichomoniasis, a common STI, is associated with low birth weight, preterm delivery, intellectual disability in children, and HIV [4][5][6]. Current tests for trichomoniasis are inaccurate and expensive [7]. This dissertation presents an investigation into using lensless optofluidic microscopy as a rapid, low-cost alternative to conventional techniques for processing urine.

Lensless microscopy offers advantages like low-cost, large field of view, and portability. By recording the image of the specimen on the detector without any intervening lenses we get a large field of view while maintaining sub-micron resolution. They are also cost effective and it allows for portability as there is no precise alignment needed. Lensless imaging can be used in combination with microfluidics to evaluate milliliters of liquid for microscopic specimen.

A common, rapid, and cost-effective test that can be done on site is the dipstick test, which is often employed in cases where urinary tract infections (UTIs) are suspected. Automated optofluidic analysis of urine has the potential to replace certain dipstick testing. Dipsticks recognize analytes that are present on or along with urine sediments; however detection of these sediments through optical analysis leads to direct identification and counting. There is also improved adherence to clinical guidelines. Microscopic hematuria, the presence of red blood cells in the urine, is defined as >3 red blood cells per high power field. Although dipsticks are able to test for red blood cells, there is still a need to have the urine examined under a microscope as well to fulfill the clinical definition. The implementation of an automated optofluidic point of care test can improve the rate of screening and diagnosis. It cannot replace dipsticks that test for chemical analytes like glucose, pH, creatinine etc.

The lensless device presented in this dissertation is a shadow imaging microscope composed of a light source, an image sensor, and a microfluidic channel. The microfluidic channel is placed in

direct contact with an image sensor and the two components are clamped together to minimize the sample-sensor distance. At 25fps the image sensor has a full field of view of 1920×1080 pixels at $1.12 \mu\text{m}$ per pixel, translating to 2.60mm^2 . The flow channel, which is 1mm in diameter, covers an area of $\sim 2.15 \text{mm}^2$. At its height of $80 \mu\text{m}$, it is able to hold $0.172 \mu\text{l}$ over the field of view. The material cost to fabricate the whole device is about \$50.

The detector chosen for our platform was a Sony IMX219PQ image sensor incorporated into a Raspberry Pi v2 camera and controlled by the Raspberry Pi 3. The ISO on the Pi v2 camera can be adjusted to a minimum gain of 1 and a maximum gain of 14.72. ISO is the gain from the sensor; it is a measure of the increase in an image's brightness after capture [8]. An increase in ISO brightens the images, but simultaneously adds noise. Due to the control over the light source, a minimal ISO is ideal for noise reduction. Other sources of noise is ambient light that may be present in the room. If there is another light source near the sensor, this could cause multiple shadows to form on the sensor from one particle. A high concentration of proteins in the urine may also cause some noise to appear in the image.

In relation to projection imaging, an ideal image sensor would have a very small pixel size ($0.5 \mu\text{m}$) in order to increase the spatial resolution and see the smallest urine sediments. It would also have a large field of view to analyze as much sample as possible in one frame. The size of the sensor can be traded off for the frame rate and flow speed. If the flow speed is high enough, the sensors frame rate must match it to capture a sharp image. The brightness of the LED can be adjusted to accommodate the frame rate and exposure time.

In order to characterize the device, numerous samples have been tested. These include polystyrene beads, Baker's yeast, whole blood, and cultured bacteria. The beads of known size demonstrated that the lensless platform slightly magnified the images of the specimen. Baker's yeast is slightly irregular in their shape and was able to retain that characteristic when imaged with the setup. Red blood cells had a characteristic tumble when travelling through the channel due to being shaped like a biconcave disk. The cultured bacteria were visible in large quantities, but individual specimen were difficult to identify. Next, we tested *Trichomonas vaginalis* parasites and urine samples that tested positive and negative for bacterial growth. *Trichomonas vaginalis* parasites can be defined by their morphology and in the future we hope to identify them based on their locomotion. Bacteria, at the moment, cannot be identified individually but can be identified when present in large amounts due to the structured noise that appears in the channel. Crystals and casts were also identified in the urine as they are very large and easily differentiable through their morphology. The larger components of urine were more easily identifiable, however the closer the size of the particle got to the limit of resolution, the less accurate the detection was. The next step in the development of an accurate diagnostic tool is to use the identifiable characteristics of each component to rapidly and accurately analyze each particle.

When imaging the polystyrene beads on the plastic thin film, a thin wetting film, which is created as the liquid medium evaporates, acts as a plano-convex micro-lens. This increases the

brightness of the bead on the sensor as the light is focused through the bead. This was used as a technique to amplify the signal of *E.coli* in Allier et al. [9]. As well, when imaged in a microfluidic channel, it is seen that the further the bead is from the sensor, the darker it appears. This indicates that the bead itself acts as a ball lens and the light's focus was shifted to above the sensor. A similar effect is seen with the pathogens in the biological experiments. For example, when *Trichomonas vaginalis* stands perpendicular to the sensor, it appears much brighter than when laying flat, perpendicular to the sensor. Certain cyanobacteria use this as a mechanism to sense light direction [10].

To our knowledge, this is the first known report of lensless imaging for urine analysis. In particular, our device demonstrated effective detection of parasites directly in urine samples without the need for concentration or culture. There have been several platforms developed and tested for culture in research labs, microbes in the environment, whole blood counting, parasite identification, and cerebrospinal fluid analysis. There has also not been any investigation into detecting free floating bacteria with lensless imaging, however detecting bacterial microcolonies on a dish has been done [11]. In terms of device hardware, the use of a clamping system to minimize the sample-sensor distance is unique to this platform and has not been seen before. Normally, the microfluidic channel is adhered to the image sensor through air plasma bonding. Our method allows for the easy replacement of microfluidic channels between samples without having to replace the image sensor.

6.2 Discussion

Successful development and implementation of this lensless imaging platform has the potential to keep the cost of diagnosis low and allow for timely feedback. We have demonstrated that it is able to simultaneously detect various pathogens in urine, making it a universal diagnostic tool. Our device has several advantages. It is the potential to be portable and cost effective; the cost to fabricate one device is ~\$80, however this can be reduced on a larger scale. The use of a microfluidic channel allows us to continuously screen for pathogens in the sample. By using shadow imaging over holographic imaging, there is no need to reconstruct images prior to detection and analysis, and the small pixel size of the detector allows for a high resolution to be able to clearly identify particles $>5\mu\text{m}$ in size. Limitations arise when imaging $1\mu\text{m}$ bacteria. As urine samples from patient to patient may be extremely diverse, the device must be able to accept every sample and discern the components within. Previously fabricated devices had the advantage of screening a fabricated sample with known components. In these cases, microfluidic channels that fit one cell at a time could be made. As urine samples from patient to patient may be extremely diverse, the device must be able to accept every sample and discern the components within. Our device is able to accept larger particulates that are found in urine like crystals and haline casts, as well as analyze smaller particles like yeast and blood cells. Despite these advantages, there are several limitations at this stage of the development process that prevent its immediate use in urine analysis.

The first limitation is the hardware challenge. Hardware challenges arise primarily from the optical clarity of the flow channel. PDMS is a sticky polymer and tends to easily attract dust and air particulates. Maintaining the optical clarity of the channel is critical to obtaining a clear image. Cells and other particulates also tend to stick to the surface of PDMS once they flow through. This biofouling can be reduced by treating the internal surface of the channel with an antifouling coating.

In terms of software, our current methods of detection are not specific to the different components of urine. Although we have illustrated that the resolution of the device is high enough to be able to visually identify specimen, and to potentially use identifiable characteristics for future processing, we are not yet at this stage. The detection strategy for *Trichomonas vaginalis* is not specific, which can lead to misidentification, and the detection limit for bacteria is too low to allow for a competitive diagnostic tool. The detection limit, sensitivity, and specificity must be characterized for the system to be compared to the gold standards of urinalysis. A direct comparison with brightfield microscopy is not possible, however, in terms of bacterial detection, an experiment can be done in which fluorescently tagged bacteria are detected with upright fluorescence microscopy and lensless microscopy simultaneously. This would allow us to achieve a ground truth for bacterial detection and help us to develop a software for automated detection.

If this device were to be implemented in other applications, beyond health care, such as in water monitoring, the detection limit would continue to be a major limitation. Sewage water contains bacterial concentrations from 10^3 to 10^5 CFU/ml as well, however surface water and ground water have much lower bacterial concentrations[12]. With our current platform we are only looking at 0.17ul in the flow channel at a time. If foreign pathogens are present in water at a concentration of less than 10^3 CFU/ml the time for detection would be very long. This can be circumvented by placing the channels in parallel on multiple image sensors and by having a larger field of view or faster frame rate.

6.3 Future Directions

This dissertation outlined the first phase in the development of a lensless shadow imaging platform for urine analysis. The next step in the development of an accurate diagnostic tool is to use the identifiable characteristics of each component in urine for automated analysis. If at the current level of hardware image processing techniques are not enough to accurately detect every component, some additions may be necessary. Bacteria can be counted via an individual bacterial examination channel, so any interference with RBCs is prevented, such as in urinary flow cytometers [13]. Another option would be to test the scattering of light by the bacteria. A laser can be implemented perpendicular to the channel and pulsed in synchronization with the white LED above. The scattering and transmission of the light through the samples can then be obtained for more information.

To further the device, a spectroscopic evaluation can be implemented to detect the type of bacteria in the channel. For instance, Raman spectroscopy has been used to identify bacteria in urine culture after a centrifugation step [14]. In this case, there can be two components to the device. The first component would analyze all of the components in blood. The sample would then be sent through a microfluidic cell sorter where the second component of the device would receive a concentrated sample of bacteria on which it could do Raman spectroscopy to determine which bacteria are in the sample. This would allow for quicker and more appropriate administration of antibiotics to patients.

The implementation of a fully automated lensless imaging platform can quickly eliminate negative samples from further processing to significantly reduce costs, and administer earlier and more appropriate treatments. It is an ideal point-of-care instrument for implementation in hospitals, clinics and nursing homes. This dissertation provided the initial steps into the development of this platform.

References

- [1] G. B. Fogazzi, *The Urinary Sediment : An Integrated View*, 3ed ed., vol. 78, no. 12. Elsevier Srl, 2010.
- [2] M. Davenport, K. E. Mach, L. M. D. Shortliffe, N. Banaei, T.-H. Wang, and J. C. Liao, “New and developing diagnostic technologies for urinary tract infections,” *Nat. Rev. Urol.*, vol. 14, no. 5, pp. 296–310, May 2017.
- [3] M. A. C. Broeren, S. Bahçeci, H. L. Vader, and N. L. A. Arents, “Screening for urinary tract infection with the Sysmex UF-1000i urine flow cytometer.,” *J. Clin. Microbiol.*, vol. 49, no. 3, pp. 1025–9, Mar. 2011.
- [4] P. Kissinger, “Trichomonas vaginalis: a review of epidemiologic, clinical and treatment issues,” *BMC Infect. Dis.*, vol. 15, no. 1, p. 307, Dec. 2015.
- [5] J. R. Mann, S. McDermott, T. L. Barnes, J. Hardin, H. Bao, and L. Zhou, “Trichomoniasis in Pregnancy and Mental Retardation in Children,” *Ann. Epidemiol.*, vol. 19, no. 12, pp. 891–899, Dec. 2009.
- [6] J. E. Allsworth, J. A. Ratner, and J. F. Peipert, “Trichomoniasis and Other Sexually Transmitted Infections: Results From the 2001–2004 National Health and Nutrition Examination Surveys,” *Sex. Transm. Dis.*, vol. 36, no. 12, pp. 738–744, Dec. 2009.
- [7] G. E. Garber, “The laboratory diagnosis of Trichomonas vaginalis.,” *Can. J. Infect. Dis. Med. Microbiol. = J. Can. des Mal. Infect. la Microbiol. medicale*, vol. 16, no. 1, pp. 35–8, Jan. 2005.
- [8] Wikipedia, “Film Speed,” *1 July 2019*. [Online]. Available: https://en.wikipedia.org/wiki/Film_speed#Current_system:_ISO.
- [9] C. P. Allier, G. Hiernard, V. Poher, and J. M. Dinten, “Bacteria detection with thin wetting film lensless imaging,” *Biomed. Opt. Express*, vol. 1, no. 3, p. 762, Oct. 2010.

- [10] N. Schuergers *et al.*, “Cyanobacteria use micro-optics to sense light direction.,” *Elife*, vol. 5, Feb. 2016.
- [11] J. H. Jung and J. E. Lee, “Real-time bacterial microcolony counting using on-chip microscopy,” *Sci. Rep.*, vol. 6, p. 21473, Feb. 2016.
- [12] P. Payment and A. Locas, “Pathogens in Water: Value and Limits of Correlation with Microbial Indicators,” *Ground Water*, vol. 49, no. 1, pp. 4–11, Jan. 2011.
- [13] P. Mejuto, M. Luengo, and J. Díaz-Gigante, “Automated Flow Cytometry: An Alternative to Urine Culture in a Routine Clinical Microbiology Laboratory?,” *Int. J. Microbiol.*, vol. 2017, pp. 1–8, Sep. 2017.
- [14] U.-C. Schröder *et al.*, “Rapid, culture-independent, optical diagnostics of centrifugally captured bacteria from urine samples.,” *Biomicrofluidics*, vol. 9, no. 4, p. 044118, Jul. 2015.
- [1] G. B. Fogazzi, *The Urinary Sediment : An Integrated View*, 3ed ed., vol. 78, no. 12. Elsevier Srl, 2010.
- [2] M. Davenport, K. E. Mach, L. M. D. Shortliffe, N. Banaei, T.-H. Wang, and J. C. Liao, “New and developing diagnostic technologies for urinary tract infections,” *Nat. Rev. Urol.*, vol. 14, no. 5, pp. 296–310, May 2017.
- [3] M. A. C. Broeren, S. Bahçeci, H. L. Vader, and N. L. A. Arents, “Screening for urinary tract infection with the Sysmex UF-1000i urine flow cytometer.,” *J. Clin. Microbiol.*, vol. 49, no. 3, pp. 1025–9, Mar. 2011.
- [4] P. Kissinger, “Trichomonas vaginalis: a review of epidemiologic, clinical and treatment issues,” *BMC Infect. Dis.*, vol. 15, no. 1, p. 307, Dec. 2015.
- [5] J. R. Mann, S. McDermott, T. L. Barnes, J. Hardin, H. Bao, and L. Zhou, “Trichomoniasis in Pregnancy and Mental Retardation in Children,” *Ann. Epidemiol.*, vol. 19, no. 12, pp. 891–899, Dec. 2009.
- [6] J. E. Allsworth, J. A. Ratner, and J. F. Peipert, “Trichomoniasis and Other Sexually Transmitted Infections: Results From the 2001–2004 National Health and Nutrition Examination Surveys,” *Sex. Transm. Dis.*, vol. 36, no. 12, pp. 738–744, Dec. 2009.
- [7] G. E. Garber, “The laboratory diagnosis of Trichomonas vaginalis.,” *Can. J. Infect. Dis. Med. Microbiol. = J. Can. des Mal. Infect. la Microbiol. medicale*, vol. 16, no. 1, pp. 35–8, Jan. 2005.
- [8] Wikipedia, “Film Speed,” 1 July 2019. [Online]. Available: https://en.wikipedia.org/wiki/Film_speed#Current_system:_ISO.
- [9] C. P. Allier, G. Hiernard, V. Poher, and J. M. Dinten, “Bacteria detection with thin wetting film lensless imaging,” *Biomed. Opt. Express*, vol. 1, no. 3, p. 762, Oct. 2010.
- [10] N. Schuergers *et al.*, “Cyanobacteria use micro-optics to sense light direction.,” *Elife*, vol. 5, Feb. 2016.
- [11] J. H. Jung and J. E. Lee, “Real-time bacterial microcolony counting using on-chip

- microscopy.,” *Sci. Rep.*, vol. 6, p. 21473, Feb. 2016.
- [12] P. Payment and A. Locas, “Pathogens in Water: Value and Limits of Correlation with Microbial Indicators,” *Ground Water*, vol. 49, no. 1, pp. 4–11, Jan. 2011.
- [13] P. Mejuto, M. Luengo, and J. Díaz-Gigante, “Automated Flow Cytometry: An Alternative to Urine Culture in a Routine Clinical Microbiology Laboratory?,” *Int. J. Microbiol.*, vol. 2017, pp. 1–8, Sep. 2017.
- [14] U.-C. Schröder *et al.*, “Rapid, culture-independent, optical diagnostics of centrifugally captured bacteria from urine samples.,” *Biomicrofluidics*, vol. 9, no. 4, p. 044118, Jul. 2015.

Appendix A: List of Supplementary Material

Supplementary Movie 1: Diluted blood flowing through the channel. The biconcave shape is an easy morphological feature to spot, and they can be seen flipping as they flow through the channel. The smaller, brighter particles in the image without the divot in the center are predicted to be damaged red blood cells. A single frame is found in Figure 4.13

Supplementary Movie 2: Raw frames of *Trichomonas vaginalis*. The flow in the channel is suspended to better understand the locomotion of the parasites.

Supplementary Movie 3: Processed frames of *Trichomonas vaginalis*. The identification algorithm is implemented to automatically identify the parasites in the channel. Some parasites are not identified in every frame. A single frame is found in Figure 5.4

Supplementary Movie 4: Urine sample negative for bacteria. A single frame is found in Figure 5.6

Supplementary Movie 5: Urine sample positive for bacteria (>100CFU). A single frame is found in Figure 5.6

Appendix B: Supplementary Figures

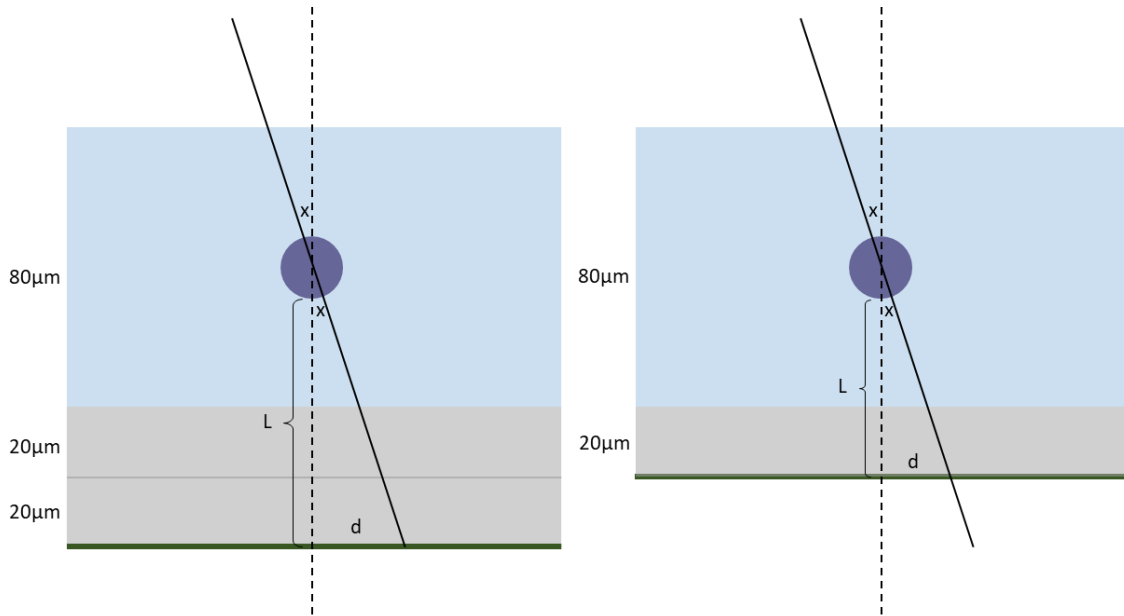


Figure 1: Effect of sample-sensor distance on shadow image. The further the distance between the sample and the sensor (L), the larger the diameter of the shadow (d).

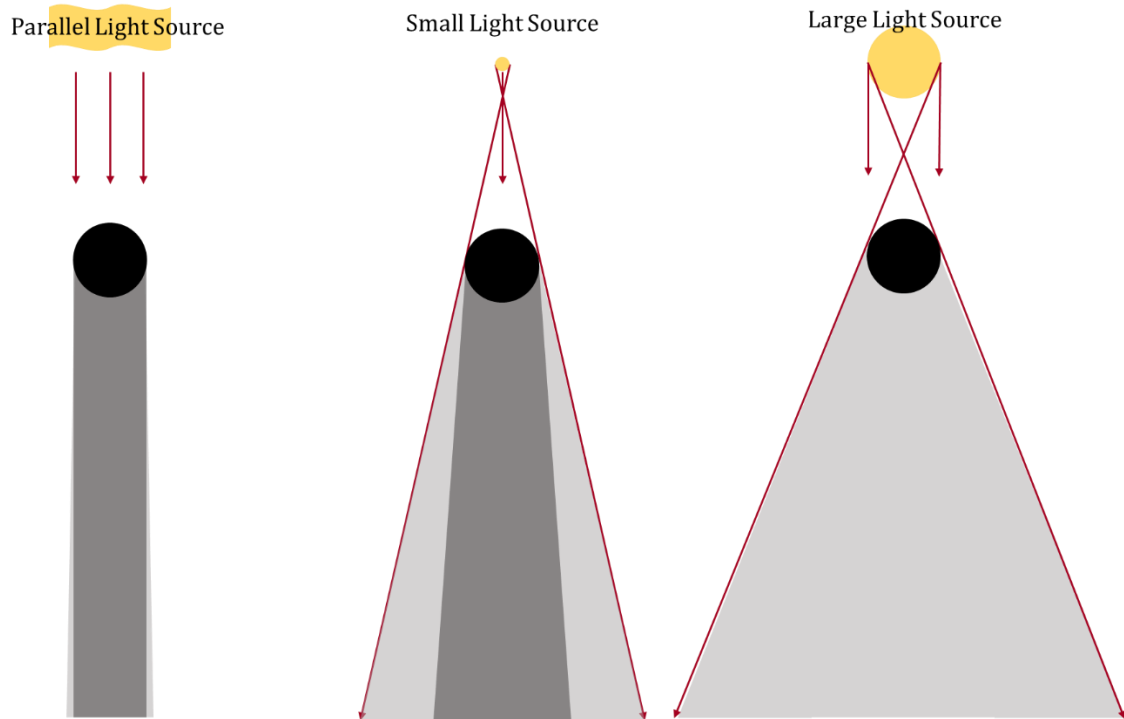


Figure 2: Effect of light source on shadow image.